ARTICLES
https://doi.org/10.1038/s41594-021-00633-2

nature structural & molecular biology

Check for updates

The tumor suppressor folliculin inhibits lactate dehydrogenase A and regulates the Warburg effect

Mark R. Woodford[1,2,3], Alexander J. Baker-Williams[1,2,3], Rebecca A. Sager[1,2,3], Sarah J. Backe[1,2,3], Adam R. Blanden[2,3], Fiza Hashmi[1,2,3], Priyanka Kancherla[1], Alessandro Gori[4], David R. Loiselle[5], Matteo Castelli[6], Stefano A. Serapian[6], Giorgio Colombo[6], Timothy A. Haystead[5], Sandra M. Jensen[7], William G. Stetler-Stevenson[7], Stewart N. Loh[2,3], Laura S. Schmidt[8,9], W. Marston Linehan[9], Alaji Bah[2,3], Dimitra Bourboulia[1,2,3], Gennady Bratslavsky[1,2,3] ✉ and Mehdi Mollapour[1,2,3] ✉

Aerobic glycolysis in cancer cells, also known as the 'Warburg effect', is driven by hyperactivity of lactate dehydrogenase A (LDHA). LDHA is thought to be a substrate-regulated enzyme, but it is unclear whether a dedicated intracellular protein also regulates its activity. Here, we identify the human tumor suppressor folliculin (FLCN) as a binding partner and uncompetitive inhibitor of LDHA. A flexible loop within the amino terminus of FLCN controls movement of the LDHA active-site loop, tightly regulating its enzyme activity and, consequently, metabolic homeostasis in normal cells. Cancer cells that experience the Warburg effect show FLCN dissociation from LDHA. Treatment of these cells with a decapeptide derived from the FLCN loop region causes cell death. Our data suggest that the glycolytic shift of cancer cells is the result of FLCN inactivation or dissociation from LDHA. Together, FLCN-mediated inhibition of LDHA provides a new paradigm for the regulation of glycolysis.

Deregulation of cellular metabolism is a prevalent and well-established hallmark of cancer[1]. Oxidative phosphorylation provides the majority of energy in many somatic cells, whereas malignant transformation generally leads to an increased reliance on glycolysis[2]. This increased glycolytic flux occurs despite the presence of oxygen, a phenomenon known as the 'Warburg effect'[3]. Cancer cells benefit from this metabolic shift by using the increased supply of NAD^+ (NAD, nicotinamide adenine dinucleotide) to support the growing demand for biosynthetic molecules provided by glycolysis. Generation of NAD^+ in glycolysis is coupled to the fermentation of pyruvate to lactate by lactate dehydrogenase A (LDHA). Previous work has demonstrated the critical importance of LDHA activity to cancer cell proliferation and, indeed, lactate generation has become a surrogate for tumorigenicity[4,5]. Despite this understanding, the factors regulating LDHA activity remain largely unexplored.

Loss of the tumor suppressor folliculin (FLCN) leads to Birt–Hogg–Dubé (BHD) syndrome, a condition characterized by cutaneous fibrofolliculomas, spontaneous pneumothorax and pulmonary cyst development, as well as renal cell carcinoma[6,7]. Canonically, FLCN participates in the regulation of mTOR through its role as a GTPase-activating protein for the GTPase RagC[8,9]. However, the precise mechanism of FLCN tumor suppressive function is unknown. Notably, it was previously shown that loss of FLCN leads to increased LDHA activity[10,11], suggesting a potential role for FLCN in the endogenous regulation of LDHA.

Results

Novel function of the tumor suppressor FLCN. FLCN is a known tumor suppressor, but its exact function remains elusive[12,13]. Our proteomic approach using FLCN-6xHis isolated from HEK293 cells identified 114 interacting proteins, including LDHA (Fig. 1a and Supplementary Table 1). Gene Ontology (GO) term enrichment analysis revealed that these FLCN-binding partners primarily belong to cellular metabolic and RNA-processing pathways (Extended Data Fig. 1a). We confirmed the interaction with LDHA by immunoprecipitation (IP) of LDHA-FLAG and co-IP of endogenous FLCN (Extended Data Fig. 1b). Immunofluorescence microscopy shows co-localization of FLCN and LDHA in HEK293 cells, further demonstrating the plausibility of this interaction (Fig. 1b). FLCN expression is inversely correlated with the activity of LDHA, as evidenced by changes in the activation-coupled phospho-Tyr10-LDHA[14,15] in response to modulation of FLCN levels (Extended Data Fig. 1c,d). These data suggest that FLCN interaction has a functional impact on LDHA activity.

LDHA and LDHB are highly conserved isoenzymes[16], and both are present endogenously in HEK293 cells. Notably, IP of LDHA- or LDHB-FLAG from whole-cell lysate showed FLCN specifically bound to LDHA, but not LDHB (Fig. 1c). We subsequently performed an IP of endogenous FLCN from haploid HAP1 cells modified by CRISPR to express either LDHA or LDHB as the sole LDH (Extended Data Fig. 2a). Co-immunoprecipitation (co-IP) of LDHA could be observed in both wild-type and LDHA-expressing cells,

[1]Department of Urology, SUNY Upstate Medical University, Syracuse, NY, USA. [2]Department of Biochemistry and Molecular Biology, SUNY Upstate Medical University, Syracuse, NY, USA. [3]Upstate Cancer Center, SUNY Upstate Medical University, Syracuse, NY, USA. [4]Istituto di Scienze e Tecnologie Chimiche 'Giulio Natta' – SCITEC, Milan, Italy. [5]Department of Pharmacology and Cancer Biology, Duke University Medical Center, Durham, NC, USA. [6]Department of Chemistry, University of Pavia, Pavia, Italy. [7]Laboratory of Pathology, Center for Cancer Research, National Cancer Institute, The National Institutes of Health, Bethesda, MD, USA. [8]Basic Science Program, Frederick National Laboratory for Cancer Research, Frederick, MD, USA. [9]Urologic Oncology Branch, Center for Cancer Research, National Cancer Institute, Bethesda, MD, USA. ✉e-mail: bratslag@upstate.edu; mollapom@upstate.edu

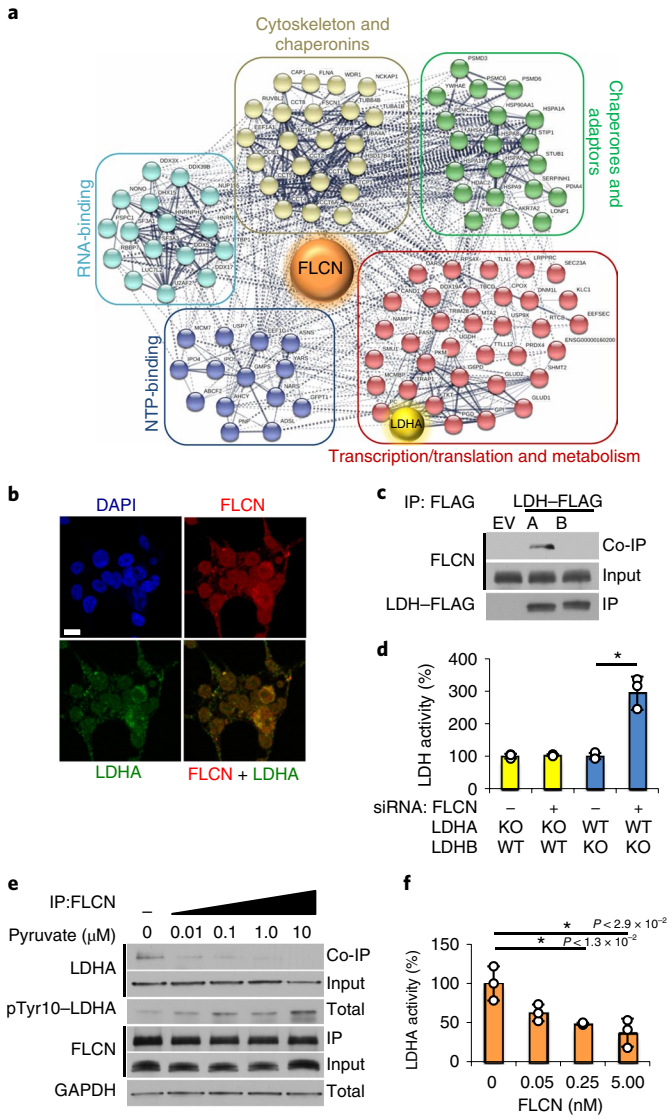

Fig. 1 | The tumor suppressor FLCN specifically binds and inhibits LDHA. **a**, FLCN-FLAG IP from HEK293 cells was subjected to matrix-assisted laser desorption/ionization-time-of-flight (MALDITOF) analysis. Colored circles are interacting proteins: green, chaperones and adaptors; red, transcription, translation and metabolism; blue, nucleotide-binding; cyan, RNA-binding; beige, chaperonins and cytoskeleton. The interactome was generated using STRING (string-db.org). **b**, Immunofluorescence imaging of HEK293 cells stained with anti-FLCN (red) and anti-LDHA (green) antibodies and DAPI (blue, nuclei). Scale bar, 10 μm. **c**, IP of LDHA-FLAG or LDHB-FLAG expressed in HEK293 cells immunoblotted with anti-FLCN to assess the interaction (co-IP). The blots are a representative example of five independent experiments. **d**, LDH activity measured in vitro using whole-cell lysates from *LDHA* or *LDHB* knockout HAP1 cells following treatment with siRNA targeting *FLCN*. Data are presented as mean ± s.d. ($n = 3$ independent samples) ($^*P < 9.0 \times 10^{-3}$, unpaired Student's *t*-test). **e**, Immunoblots of anti-FLCN IPs and whole-cell extracts following exogenous addition of pyruvate to HEK293s (treatment duration of 6 h). The blots are a representative example of three independent experiments. **f**, Activity of 10 nM recombinant LDHA measured in the presence of increasing amounts of recombinant FLCN. Data are presented as mean ± s.d. ($n = 3$ independent samples). *P* values based on unpaired Student's *t*-test: $^*P < 0.05$. Source data for **c**–**f** are available online.

but no interaction with LDHB was detected (Extended Data Fig. 2a). Additionally, suppressing FLCN expression using siRNA (Fig. 1d and Extended Data Fig. 2b) enhanced the activity of LDHA, but not LDHB, suggesting FLCN specifically binds and regulates LDHA activity (Fig. 1d).

LDHA and LDHB are known to form mixed tetrameric complexes described as a 'dimer of dimers'[14,15,17,18]. Consecutive IP of co-expressed LDHA-HA/LDHA-FLAG or LDHA-HA/LDHB-FLAG demonstrated FLCN interaction with LDHA/LDHA homodimers but not LDHA/LDHB heterodimers (Extended Data Fig. 2c). LDHA also forms higher-order oligomers in cells observable by native polyacrylamide gel electrophoresis (PAGE)[19], which probably correspond to the tetrameric and dimeric states of LDHA reported previously[20]. Our data showed that overexpression of FLCN corresponds to a decrease in large oligomeric complexes of LDHA (Extended Data Fig. 2d,e) and induces formation of a dimeric LDHA species (70 kDa; Extended Data Fig. 2e). We then immunoprecipitated FLCN-FLAG and observed interaction with this dimer of LDHA (70 kDa; Extended Data Fig. 2e).

To interrogate the mechanism of FLCN selectivity for LDHA, we developed chimeric constructs based on the concentration of natural sequence and structural variation in the first 22 (N) and last 38 (C) amino acids of LDHA and LDHB (Extended Data Fig. 3a,b)[21]. Exchanging the LDHB N domain or C domain individually into LDHA preserved binding of FLCN (Extended Data Fig. 3c). However, replacing both domains (NC) completely abrogated FLCN interaction, similar to wild-type LDHB (Extended Data Fig. 3c). These observations further reinforce the inherent specificity of FLCN for LDHA over LDHB.

Canonically, LDHA is activated in cells by pyruvate accumulation[22,23]. To evaluate whether the activation of LDHA is coupled to its dissociation from FLCN, we treated HEK293 cells with physiological concentrations of pyruvate. LDHA activation resulted in disruption of the FLCN–LDHA complex, as co-IP of LDHA with FLCN was primarily observed at the lowest doses of exogenous pyruvate (Fig. 1e and Extended Data Fig. 4a). Notably, addition of lactate had a much milder effect on dissociation of LDHA from FLCN (Extended Data Fig. 4b), consistent with LDHA preference for pyruvate as a substrate[24]. Pre-incubation of LDHA with recombinant FLCN also attenuates LDHA activity in vitro (Fig. 1f), suggesting that the FLCN–LDHA interaction precludes substrate binding.

We next examined the impact of FLCN on NADH cofactor binding to LDHA. NADH binding in the active site of LDHA is a prerequisite for substrate binding. The dye Cibacron Blue 3GA (Cib) is often used for affinity-purification of enzymes that contain NADH cofactor binding sites[25]. LDHA binding to Cib-agarose was greatly diminished in HEK293 cells overexpressing FLCN, suggesting FLCN interference with cofactor binding to LDHA (Extended Data Fig. 4c). Together, our data suggest that the tumor suppressor FLCN specifically binds to LDHA, but not LDHB[26], and inhibits its enzymatic activity.

FLCN uncompetitively inhibits LDHA. To determine the molecular mechanism of FLCN-mediated inhibition of LDHA, we constructed, transiently expressed, and immunoprecipitated a series of FLCN truncation mutants in HEK293 cells. We identified amino acids (aa) 210–220 within FLCN to be essential for interaction with LDHA (Extended Data Fig. 5a–d). On the basis of the published cryo-EM structures, this region of FLCN falls within an unstructured loop positioned between two α-helices in the N terminus (Fig. 2a)[8,27]. We subsequently made a series of overlapping peptides including addition or removal of upstream or downstream amino acids, point mutations and T227 phosphorylation beginning with aa 220–230, as these residues are definitively within the LDHA-binding region (Fig. 2b and Extended Data Fig. 5d). We demonstrated that this peptide derived from aa 220–230 (FLCN-1) bound tightly to LDHA ($K_a \approx 1 \times 10^7\ M^{-1}$; Extended Data Fig. 5e). Encouragingly, peptide-10 (FLCN-10; aa 219–228) showed greatly enhanced binding (Fig. 2c) and had a strong inhibitory effect on LDHA activity

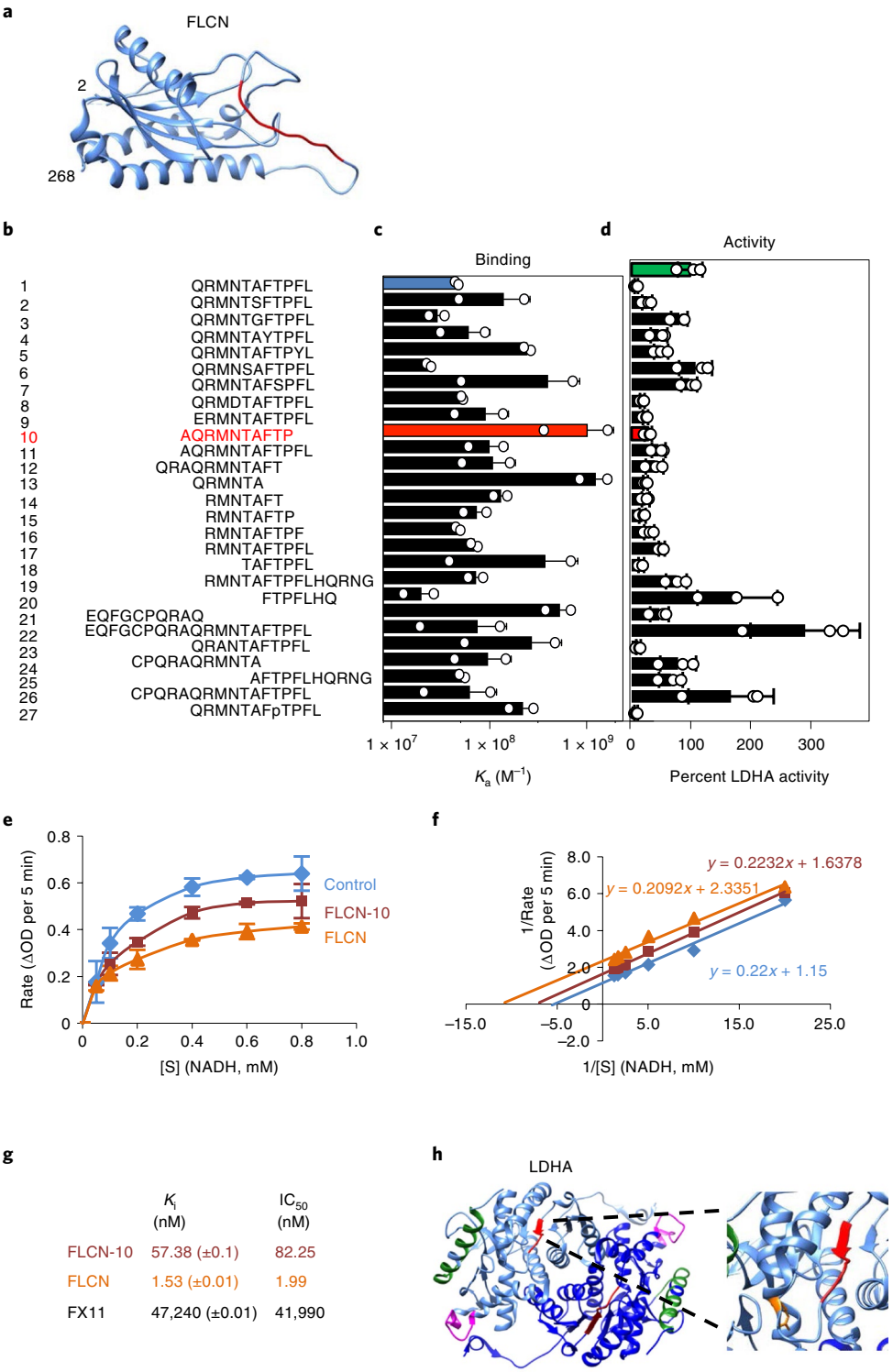

	K_i (nM)	IC_{50} (nM)
FLCN-10	57.38 (±0.1)	82.25
FLCN	1.53 (±0.01)	1.99
FX11	47,240 (±0.01)	41,990

Fig. 2 | A decameric peptide of FLCN uncompetitively inhibits LDHA. a, Structure of the FLCN N terminus solved by cryo-EM (aa 2–268; PDB 6NZD). The FLCN-10 peptide is highlighted in red. **b**–**d**, List of synthetic FLCN peptides (**b**) screened for K_a by fluorescence polarization anisotropy (**c**) or ability to inhibit LDHA (**d**) in vitro. The green bar represents the activity of LDHA alone (100%). LDHA activity is highlighted in the presence of FLCN-1 (blue) and FLCN-10 (red). Data are presented as mean ± s.d. ($n = 3$ independent samples). **e**, Michaelis–Menten kinetics of LDHA activity alone or in the presence of FLCN protein or FLCN-10 peptide. [S] is the concentration of NADH. Data are presented as mean ± s.d. ($n = 3$ independent samples). **f**, Enzyme kinetic data presented as a Lineweaver–Burk plot ($n = 3$ independent samples). **g**, Measured values for LDHA binding and kinetic data from this figure and Extended Data Fig. 6a–e. **h**, Structure of dimeric LDHA, with individual monomers colored light or dark blue (PDB 4OKN). Limited proteolysis-coupled mass spectrometry (MS) identified LDHA catalytic-loop-region perturbation (red) and loss of antigenic-loop accessibility (magenta) in response to FLCN-10 peptide binding. The green α-helix represents peptides unchanged by the presence of FLCN-10. The LDHA catalytic R106 is highlighted in orange (inset). Structures were rendered using Chimera v1.12 (UCSF). Source data for **c**–**f** are available online.

(70%) (Fig. 2d). These data are summarized in a plot of K_a against LDHA activity in Extended Data Fig. 5f.

Previous work has shown that tetramerization of LDHA is largely dependent on concentration in vitro and that tetrameric LDHA displays increased activity[20]. Treatment of predominantly dimeric (10 ng µl^{-1}) or tetrameric LDHA (500 ng µl^{-1}) with recombinant FLCN protein or FLCN-10 peptide demonstrates that FLCN is able to effectively inhibit dimeric, but not tetrameric, LDHA (Extended Data Fig. 5g,h), in agreement with our earlier findings (Extended Data Fig. 2c–e). Using traditional enzyme kinetics, we further showed that FLCN-10 uncompetitively inhibits LDHA (Fig. 2e,f and Extended Data Fig. 6a,b). Both full-length FLCN protein and FLCN-10 peptide also showed greatly improved potency as compared to the previously characterized LDHA inhibitor FX11[4] (Extended Data Fig. 6c–f). The binding and kinetic data are summarized in Fig. 2g.

Limited proteolysis-coupled mass spectrometry (LiP-MS) is a technique by which proteolytic cleavage can be used to observe structural changes in a protein induced by small-molecule interaction[28]. Following digestion with trypsin, which cleaves after lysine and arginine residues, a complex of FLCN-10 peptide with full-length recombinant LDHA yielded one unique differential LDHA peptide corresponding to residues 91-LVIITAGAR-99, which forms the N-terminal portion of the LDHA catalytic loop (Fig. 2h and Supplementary Table 2)[29]. Accessibility of the LDHA catalytic loop is probably altered as a result of allosteric effects on the active site secondary to FLCN binding. This is consistent with FLCN interference with cofactor (NADH) binding and uncompetitive inhibition of LDHA. Interestingly, proteolytic sensitivity was lost for the LDHA peptide 213-TLHPDLGTDKDKEQWK-228 following FLCN-10 peptide treatment (Fig. 2h and Supplementary Table 2). This exposed, flexible region contains the 'antigenic loop' of LDHA, so named because it harbors sufficient variation to differentiate LDH isoforms[30]. Although distal from the active-site pocket (25 Å; ref. [16]), this region may play a role in the ability of FLCN discrimination between LDH isoforms.

On the basis of the crystal structure of LDHA, arginine-106 is within its catalytic loop and is important for its activity, and mutation of R106 to alanine, lysine or glutamine has been shown to restrict movement of the catalytic loop[31]. These mutants showed increased binding to FLCN (Extended Data Fig. 6g). Additionally, streptavidin pulldown of a biotinylated FLCN-10 analog demonstrated enhanced binding to these inactive LDHA mutants (Extended Data Fig. 6g). Therefore, our data suggest that FLCN binding can be modulated by changes in the LDHA active site.

FLCN regulates glycolysis. FLCN is a modular protein consisting of an N-terminal intrinsically disordered region (IDR), followed by two structured domains that are linked by a long IDR loop[8,27,32]. The identified LDHA-binding residues are located on this IDR loop, composed of residues 216–248 of FLCN (Fig. 3a). To gain further insight into the mechanism of FLCN binding and inhibition of LDHA, we made a series of mutations within the FLCN-10 peptide region of full-length FLCN. Each residue was mutated independently to alanine, with the exception of the two naturally occurring alanine residues (A219 and A225), which were mutated to asparagine (Fig. 3b). Several mutations in FLCN appeared to completely abrogate binding to LDHA, including R221A, F226A and P228A (Fig. 3c). Notably, only one mutation (M222A) markedly increased the binding of FLCN to LDHA (Fig. 3c).

BHD syndrome is caused by mutation and inactivation of *FLCN* and predisposes patients to renal cell carcinoma[33]. We examined the function of the FLCN-M222A mutant by expressing two different amounts of FLCN-WT-FLAG (WT, wild type) and FLCN-M222A-FLAG in the UOK257 cell line (Extended Data Fig. 7a), which is a *FLCN*-null cell line established from a patient with BHD syndrome[10,34]. Transient transfection of 2 µg of FLCN-WT or FLCN-M222A plasmid had little effect on extracellular acidification rate (ECAR), a measure of glycolytic flux (Fig. 3d). However, transfection of 8 µg of either construct reduced ECAR to a similar level as the FLCN-replaced control cell line, UOK257-2 (Fig. 3d). In parallel, we collected lysates from these transfections to assess their LDH activity. We observed LDH activity reduced to ~77% upon transfection of 2 µg of FLCN-WT, and a statistically significant further reduction in LDH activity (~51%) upon transfection of 2 µg FLCN-M222A ($P < 0.0001$; Fig. 3e). This decreased LDH activity is similar to that achieved by expressing 8 µg of FLCN-WT (Extended Data Fig. 7c), suggesting a much greater inhibitory effect of FLCN-M222A. These results were reinforced by the FLCN-F226A mutation, which lacked interaction with LDHA. Consequently, 2 µg of FLCN-F226A transfection had a minimal effect on ECAR and LDHA activity (Fig. 3c–e and Extended Data Fig. 7b). Overexpression of 8 µg of FLCN-F226A, however, appears to have saturated the cellular system, leading to a reduction in LDHA activity. It is noteworthy that this data point should be viewed as control and not the true dynamic of the FLCN–LDHA interaction.

Similarly, FLCN-M222A demonstrated increased ability to suppress anchorage-independent growth of UOK257 cells in soft agar, whereas the FLCN-F226A was less effective (Fig. 3f and Extended Data Fig. 7c,d). Together, the M222A and F226A mutants demonstrated that the inhibitory function of FLCN toward LDHA correlates with FLCN:LDHA binding affinity in cells.

Recent reports have demonstrated the role of FLCN-F118 in the assembly of the Ragulator complex[8] and FLCN-R164 in the GTPase-activating protein (GAP) activity of FLCN[27], both of which are outside the identified LDHA binding region. Interestingly, neither FLCN-F118D nor R164A mutation affected the FLCN-mediated inhibition of LDHA in HEK293 cell lysates, suggesting exclusivity of these reported FLCN functions (Extended Data Fig. 7e).

FLCN inhibition of LDHA is commonly lost in cancer. It is well established that kidney cancers, in general, experience the Warburg effect[35]. We found FLCN expression levels reduced in clear cell renal cell carcinoma (ccRCC) cell lines compared to HEK293 control cells, and these ccRCC cell lines demonstrated hyperactive LDHA (Fig. 4a). We further observed that FLCN dissociation from LDHA in ccRCC correlated with increased LDHA activity (Fig. 4a). We also evaluated whether this dissociation was coupled to a change in the oligomeric state of LDHA. Consistent with our previous observations, these ccRCC cell lines demonstrated increased LDHA tetramer:dimer ratios that were inversely correlated with FLCN:LDHA interaction (Fig. 4b).

As shown in Fig. 3c, FLCN-M222A displays enhanced binding to LDHA. FLCN-M222A retains the ability to bind LDHA when expressed in ccRCC, bypassing the potential regulatory signaling governing this loss of interaction in kidney cancer (Fig. 4c). We then sought to determine whether dissociation of FLCN from LDHA was a common feature of cancer cells. Across a panel of 12 cancer cell lines, 10 demonstrated an increased phospho-Tyr10-LDHA:FLCN ratio, supporting a link between decreased FLCN expression and increased LDHA activity across cancers (Fig. 4d,e). Immunoprecipitation of endogenous LDHA from these cancer cell lines confirmed this link, demonstrating a decreased ability of FLCN to interact with LDHA in cancer (Fig. 4e,f). Together, our data demonstrate FLCN:LDHA dissociation to be a common trait of cancer cells experiencing the Warburg effect.

FLCN peptide inhibits LDHA and induces apoptosis in cancer cells. LDHA is an appealing therapeutic target, although inhibitors have not meaningfully progressed beyond preclinical evaluation[36]. Given this, we asked whether any of our screened peptides (Fig. 2b) were efficacious in cells. We selected a number of candidate

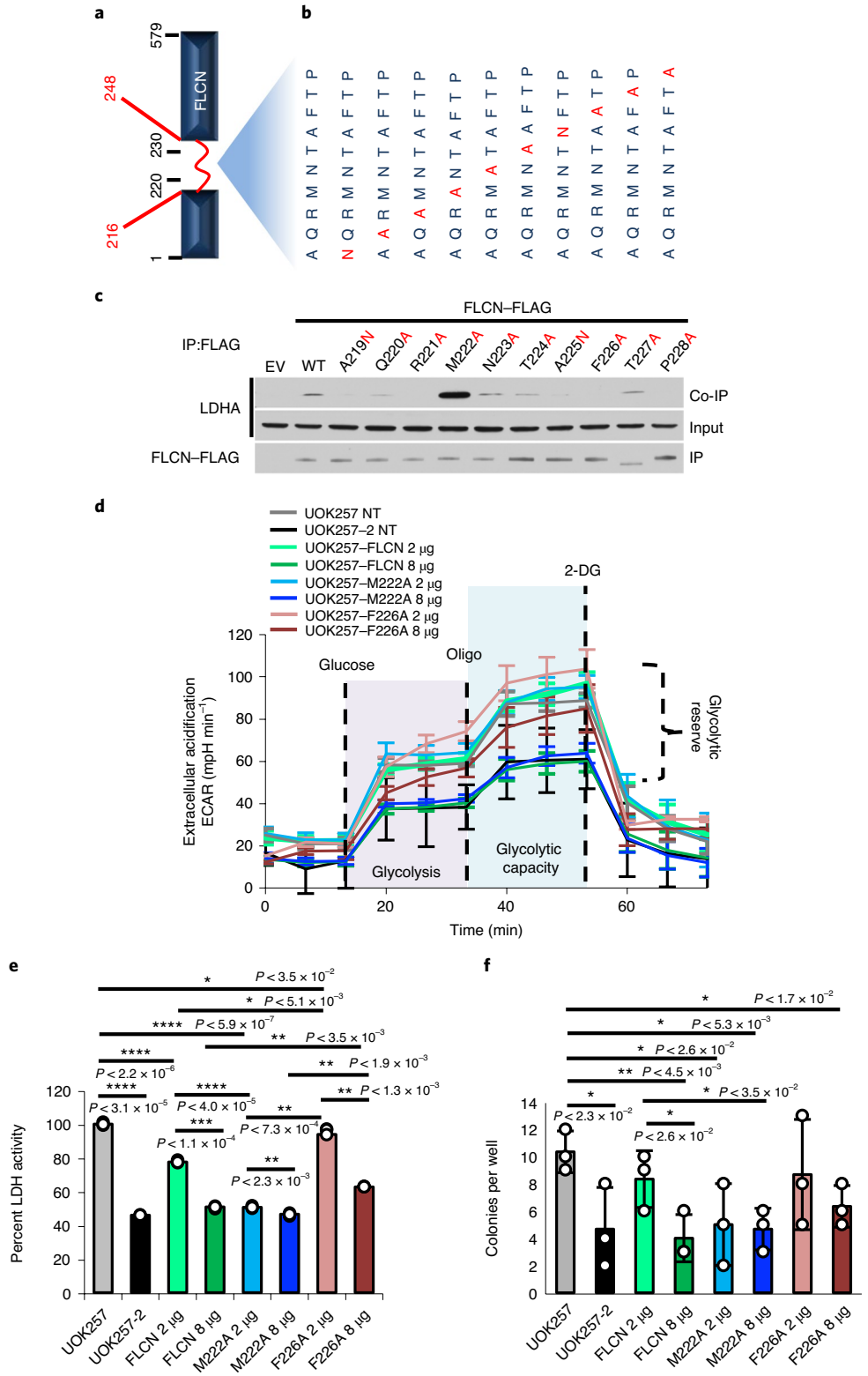

Fig. 3 | FLCN regulates glycolysis. a, Schematic of the FLCN protein, highlighting the flexible loop region (red; aa 216–248). **b**, Individual amino acid mutations in full-length FLCN within the region corresponding to FLCN-10. **c**, FLAG-tagged FLCN protein harboring point mutations within the FLCN peptide region were transiently expressed in HEK293 cells and immunoprecipitated. The interaction with LDHA (co-IP) was assessed by immunoblot. The blots are a representative example of three independent experiments. **d**, Extracellular acidification rate of UOK257 cells transfected with 2 µg or 8 µg of WT FLCN, M222A or F226A mutants. Data are presented as mean ± s.d. ($n = 8$ independent samples). **e**, LDH activity of lysates collected from samples analyzed in Extended Data Fig. 7a,b. Data are presented as mean ± s.d. ($n = 3$ independent samples). Asterisks indicate P values based on unpaired Student's t-test. *$P < 0.05$; **$P < 0.01$; ***$P < 0.001$; ****$P < 0.0001$. **f**, Soft agar assay of UOK257 cells expressing indicated FLCN-FLAG. The bar chart shows colonies counted per well. Data are presented as mean ± s.d. ($n = 3$ independent samples). Asterisks indicate P values based on unpaired Student's t-test. Source data for **c**–**f** are available online.

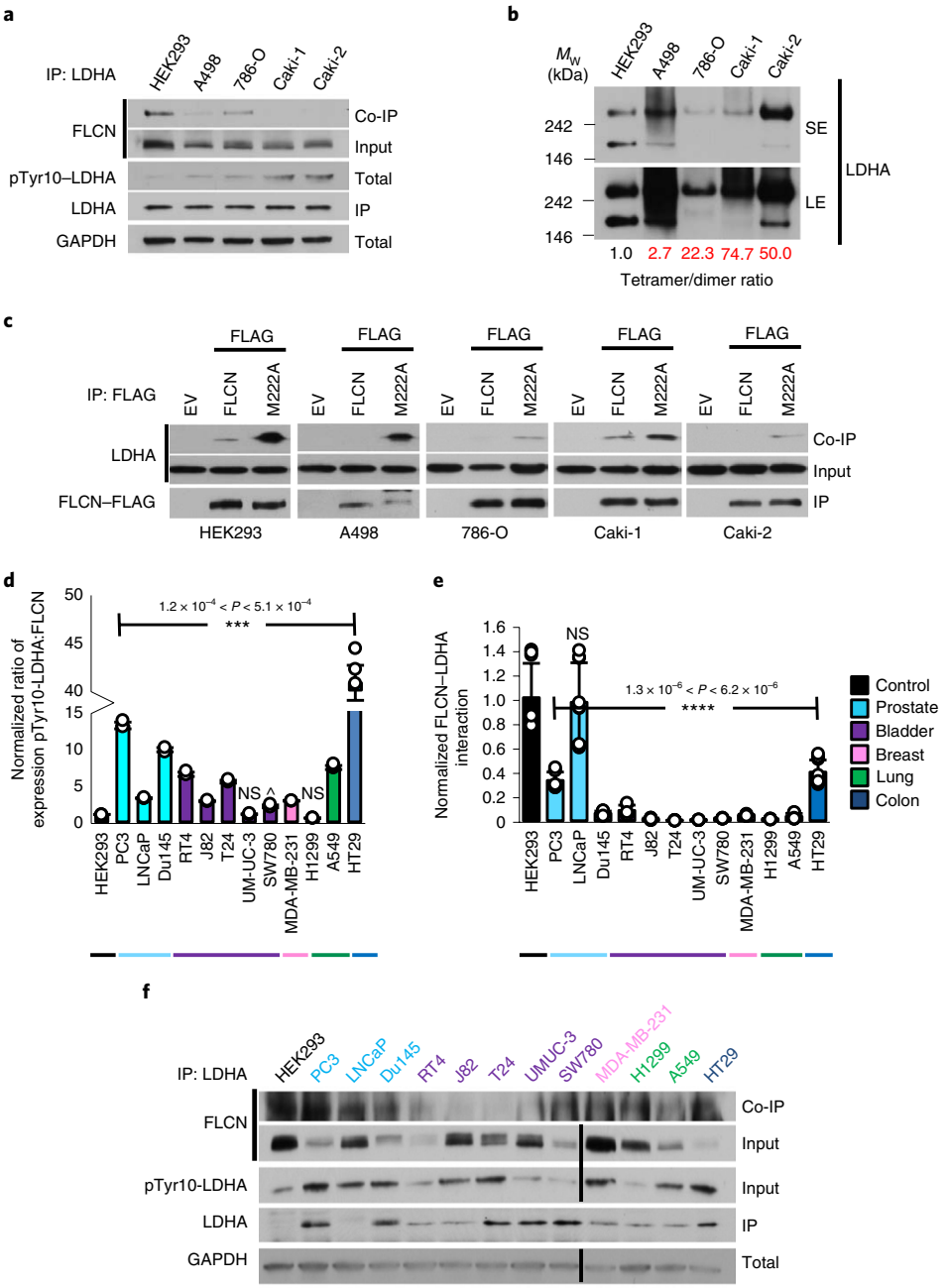

Fig. 4 | FLCN inhibition of LDHA is commonly lost in cancer. a, IP of endogenous LDHA with an anti-LDHA antibody from renal cell lines. Interaction with FLCN was observed by immunoblot. The blots are a representative example of three independent experiments. **b**, Native western blot of renal cell lysate, immunoblotted using anti-LDHA antibody. SE, short exposure; LE, long exposure. The blots are a representative example of three independent experiments. **c**, IP of WT FLCN and M222A FLCN mutant expressed in renal cell lines. Interaction with LDHA was observed by immunoblot. The blots are a representative example of three independent experiments. **d**, Densitometric ratio of normalized pTyr10-LDHA:FLCN expression in a panel of cancer cell lines. Data are presented as mean ± s.d. ($n = 3$ independent samples). *P* values based on unpaired Student's *t*-test: $^{***}P < 0.001$; NS, not statistically significant; $^{\wedge}P < 6.9 \times 10^{-2}$. **e**, Normalized FLCN–LDHA interaction from a panel of cancer cell lines. Data are presented as mean ± s.d. ($n = 3$ independent samples). *P* values based on unpaired Student's *t*-test: $^{****}P < 0.0001$. **f**, Immunoblots of endogenous FLCN and pTyr10-LDHA and interaction of FLCN and LDHA in a panel of cancer cell lines. Source data for all panels are available online.

peptides labeled with rhodamine B and evaluated their cell permeance using fluorescence microscopy (Extended Data Fig. 8a). We found that several of the candidate peptides were taken up by cells, including the two most potent in vitro, FLCN-10 and FLCN-13 (Extended Data Fig. 8a). In parallel, we examined whether these peptides were able to reduce the activity of LDHA in HEK293 cells. Interestingly, rhodamine B-labeled FLCN-1, FLCN-3 and FLCN-10 peptides effectively reduced LDHA activity, whereas FLCN-13 had only a modest effect (Extended Data Fig. 8b).

Previous work has established that inhibition of LDHA in Warburg-shifted cells induces apoptosis[4]. We subsequently examined whether these peptides could impact survival of ccRCC cell lines. Indeed, FLCN-10 peptide demonstrated the ability to suppress LDHA activity and induce cell death in ccRCC cell lines

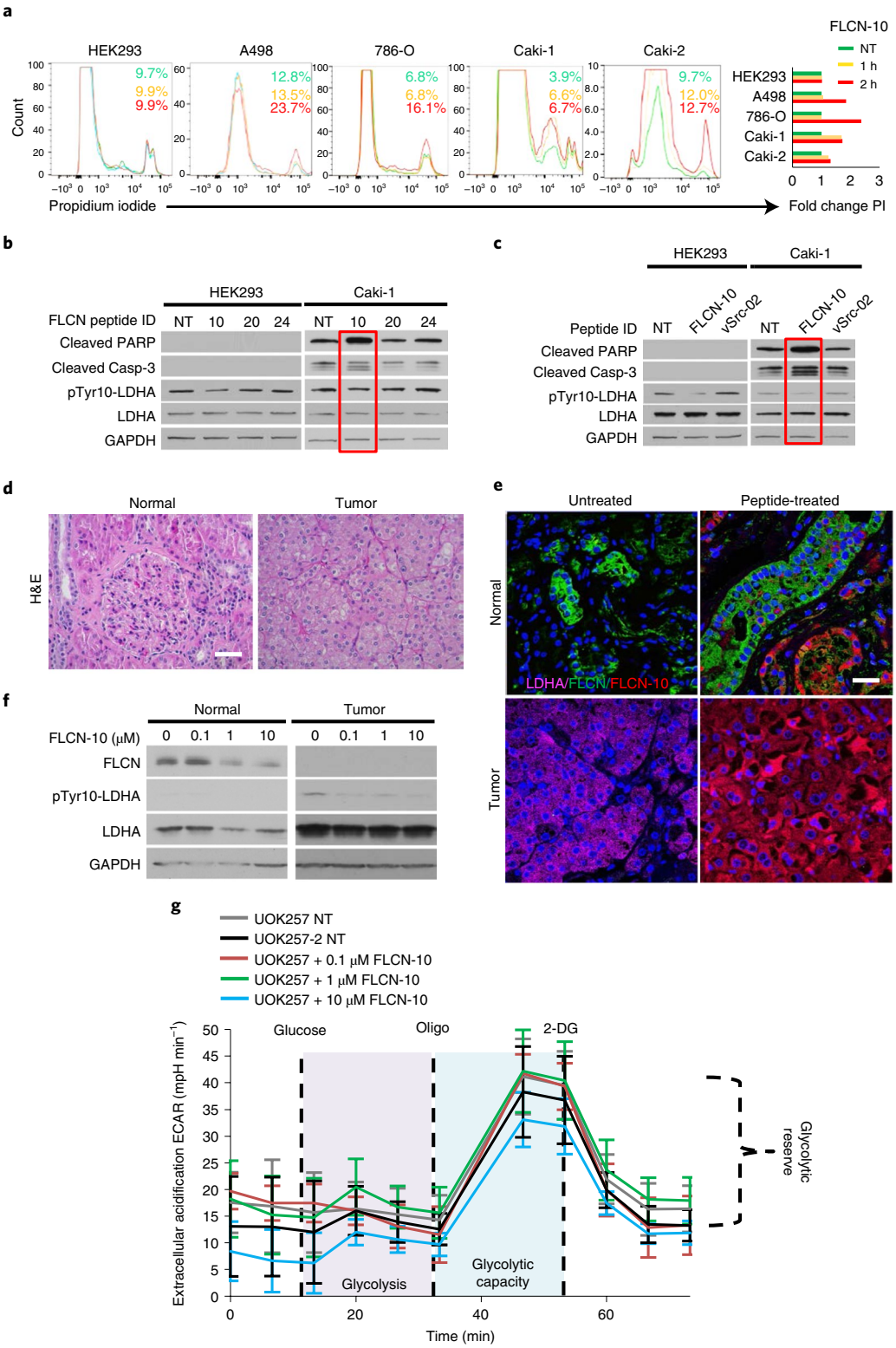

Fig. 5 | FLCN peptide inhibits LDHA and induces apoptosis in cancer cells. a, Flow-cytometric assessment of cell death in renal cell lines following treatment with 1 μM FLCN-10 for 1 h (yellow) or 2 h (red), as determined by propidium iodide staining. Green indicates no treatment (NT). A representative of three independent experiments is shown. **b**, Immunoblot of whole-cell lysates from HEK293 and Caki-1 cells following 1 μM treatment with the indicated FLCN peptides for 2 h. The blots are a representative example of three independent experiments. **c**, Immunoblot of whole-cell lysates from HEK293 and Caki-1 cells following 1 μM treatment with either FLCN-10 or vSrc-02 peptide for 2 h. **d**, Hematoxylin and eosin (H&E) staining of normal and tumor renal tissues from a patient with BHD. Scale bar, 40 μm. **e**, Fluorescence microscopy of normal and tumor renal tissues from a patient with BHD treated ex vivo with FLCN-10–rhodamine B and stained with anti-FLCN (green), anti-LDHA (pink) and DNA (Hoechst 33258; blue) Scale bar, 20 μm. **f**, Western blots of whole-cell lysates collected from **e**. **g**, Extracellular acidification rate of UOK257 cells treated with increasing amounts of FLCN-10 peptide for 2 h. Data are presented as mean ± s.d. ($n = 4$ independent samples). Source data for **b**, **c**, **f** and **g** are available online.

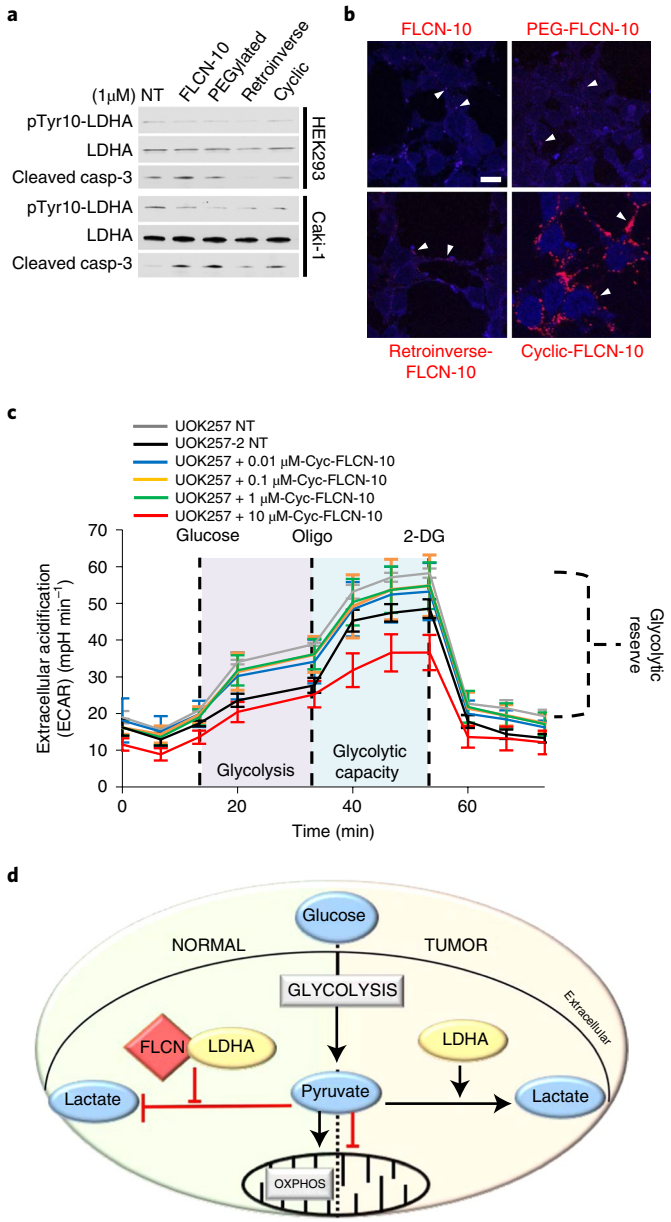

Fig. 6 | Model of FLCN-mediated regulation of LDHA. a, Western blot of pTyr10-LDHA and cleaved caspase-3 in HEK293 and Caki-1 cells following treatment with modified FLCN peptides. NT, no treatment. The blots are a representative example of three independent experiments. **b**, Fluorescence imaging of modified rhodamine B-labeled FLCN-10 peptides in HEK293 cells. White arrowheads denote examples of FLCN-10 localization. Scale bar, 10 μm. **c**, Extracellular acidification rate of UOK257 cells treated with increasing doses of cyclic-FLCN-10 peptide for 2 h. Data are presented as mean ± s.d. $n = 6$ independent samples. **d**, In normal cells, FLCN regulates the activity of LDHA. In cancer cells experiencing the Warburg effect, FLCN and LDHA have lost the ability to interact, leading to the hyperactivity of LDHA. Source data for **a** and **c** are available online.

(Extended Data Fig. 9a). Importantly, FLCN-10 does not affect the survival of control HEK293 cells, despite LDHA inhibition (Fig. 5a and Extended Data Fig. 9b–d). As controls, we tested FLCN-13 (reduced cell permeability), FLCN-20 (inability to bind and inhibit LDHA), FLCN-24 (inability to inhibit LDHA) and c-Src-02[37] (unrelated, cell-permeable negative control peptide) and showed that these peptides were unable to induce apoptosis (Fig. 5b,c).

We then asked whether overexpression of full-length *FLCN* would cause apoptosis in ccRCC cells. Interestingly, although wild-type FLCN expression induced apoptosis in ccRCC cells, the M222A mutation, which confers greater binding and inhibition of LDHA, did not further increase apoptosis (Extended Data Fig. 9e). As expected, the FLCN-F226A mutant, which does not bind to LDHA, was unable to induce apoptosis in ccRCC, demonstrating that FLCN binding to and inhibition of LDHA is necessary to mediate this effect (Extended Data Fig. 9e). Surprisingly, the corresponding FLCN-M222A peptide (FLCN-10A) was cell impermeable and had no activity against LDHA in Caki-1 cells (Extended Data Fig. 9f,g).

FLCN-10 peptide is cell-permeable and can inhibit LDHA in vitro and in cells (Fig. 2d and Extended Data Figs. 8a and 9a,b). We therefore ex vivo-treated renal tumor tissue and adjacent normal kidney tissue from a patient with BHD harboring a pathogenic *FLCN* mutation with FLCN-10 peptide (Fig. 5d). Our data revealed that FLCN-10 peptide is able to penetrate both normal and tumor tissues (Fig. 5e) and effectively inhibit LDHA ex vivo, as evidenced by a reduction in phospho-Tyr10-LDHA (Fig. 5f).

To determine whether FLCN-10 peptide compensated for a lack of FLCN-mediated inhibition of LDHA, we returned to the FLCN-null patient-derived UOK257 cell model. A modest decrease in ECAR was observed following treatment with FLCN-10 peptide (Fig. 5g), suggesting FLCN-10 peptide can recapitulate FLCN function with regard to LDHA inhibition.

Despite this encouraging result, it is well known that linear peptides are notoriously unreliable as therapeutic effectors[38]. We therefore created a series of modified FLCN-10 peptides to confer protection from cellular proteases. Our data showed that the PEGylated, Retroinverse and heterocyclic FLCN-10 peptides were effective at inhibiting LDHA activity (Fig. 6a). However, the heterocyclic FLCN-10 peptide showed increased cell penetrance (Fig. 6b and Extended Data Fig. 10a), and treatment with this modified peptide induced cell death in ccRCC (Extended Data Fig. 10b,c), as well as a potent, dose-dependent decrease in ECAR (Fig. 6c). Taken together, cyclization is an effective modification for protecting FLCN-10 peptide while preserving its activity, suggesting potential therapeutic utility that warrants further investigation.

In summary, we have characterized FLCN as a specific regulator of LDHA activity in normal cells (Fig. 6d). We subsequently identified a decapeptide within the amino domain of FLCN that is able to enter cancer cells and patient tumors and selectively inhibit LDHA activity, resulting in cell death.

Discussion

LDHA follows an ordered sequential mechanism whereby NADH binding to the co-factor-binding site precedes binding of pyruvate to the substrate-binding site. A subsequent conformational change in which the active-site loop closes over the active site provides a largely desolvated ternary complex. Our orthogonal approach has identified the tumor suppressor FLCN as a bona fide endogenous uncompetitive inhibitor of LDHA. Mechanistically, it appears that FLCN prefers binding to the less active LDHA dimer, compared to the hyperactive LDHA tetramer. A flexible loop within the amino terminus of FLCN controls movement of the LDHA active-site loop, which tightly regulates its enzyme activity and consequently metabolic homeostasis in normal cells. A protease-sensitive flexible antigenic loop within the substrate-binding domain of LDHA may also confer specificity of FLCN for LDHA.

Germline mutations in the tumor suppressor *FLCN* cause BHD syndrome, which predisposes affected individuals to develop kidney tumors. Previous works have shown that loss of *FLCN* causes dysregulation of LDHA and high lactate production in patient-derived cell lines[10,11]. Our data suggest that pathogenic mutation of *FLCN* enables LDHA hyperactivity as a result of a lack of direct LDHA inhibition by FLCN, leading to a metabolic shift in these tumors. FLCN is also

unable to bind and inhibit LDHA in cancer cells that experience the Warburg effect. Interestingly, FLCN mutation rate is low across cancers[39–43], suggesting a prevalent and robust epigenetic and/or post-translational inactivation. Although we do not know the signaling mechanisms that govern FLCN binding and/or dissociation from LDHA, we have managed to bypass this regulatory mechanism using a small FLCN-derived decapeptide that is cell-permeant and sufficient to efficiently inhibit LDHA activity. This decapeptide also has the ability to inhibit LDHA in a tumor derived from a patient with BHD.

LDHA is hyperactive in cancer cells experiencing the Warburg effect. Characteristically, LDHA is tetramerized in these cells, and binding to FLCN is less favorable in this state. However, the FLCN decapeptide has the ability to bind and inhibit LDHA in these cancer cells. Importantly, LDHA inhibitors have yet to see meaningful clinical advancement, in part due to a lack of isoform selectivity[44]. The inherent specificity of FLCN for LDHA over LDHB provides a conceptual advantage for future drug development efforts. Recapitulation of FLCN-mediated LDHA inhibition may be a new avenue for targeted therapy in these cancers.

Online content

Any methods, additional references, Nature Research reporting summaries, source data, extended data, supplementary information, acknowledgements, peer review information; details of author contributions and competing interests; and statements of data and code availability are available at https://doi.org/10.1038/s41594-021-00633-2.

Received: 30 September 2020; Accepted: 29 June 2021;
Published online: 11 August 2021

References

1. Hanahan, D. & Weinberg, R. A. Hallmarks of cancer: the next generation. *Cell* **144**, 646–674 (2011).
2. Epstein, T., Gatenby, R. A. & Brown, J. S. The Warburg effect as an adaptation of cancer cells to rapid fluctuations in energy demand. *PLoS ONE* **12**, e0185085 (2017).
3. Warburg, O., Wind, F. & Negelein, E. The metabolism of tumors in the body. *J. Gen. Physiol.* **8**, 519–530 (1927).
4. Le, A. et al. Inhibition of lactate dehydrogenase A induces oxidative stress and inhibits tumor progression. *Proc. Natl Acad. Sci. USA* **107**, 2037–2042 (2010).
5. Fantin, V. R., St-Pierre, J. & Leder, P. Attenuation of LDH-A expression uncovers a link between glycolysis, mitochondrial physiology and tumor maintenance. *Cancer Cell* **9**, 425–434 (2006).
6. Birt, A. R., Hogg, G. R. & Dubé, W. J. Hereditary multiple fibrofolliculomas with trichodiscomas and acrochordons. *Arch. Dermatol.* **113**, 1674–1677 (1977).
7. Schmidt, L. S. & Linehan, W. M. FLCN: the causative gene for Birt–Hogg–Dubé syndrome. *Gene* **640**, 28–42 (2018).
8. Lawrence, R. E. et al. Structural mechanism of a Rag GTPase activation checkpoint by the lysosomal folliculin complex. *Science* **366**, 971–977 (2019).
9. Napolitano, G. et al. A substrate-specific mTORC1 pathway underlies Birt–Hogg–Dubé syndrome. *Nature* **585**, 597–602 (2020).
10. Preston, R. S. et al. Absence of the Birt–Hogg–Dubé gene product is associated with increased hypoxia-inducible factor transcriptional activity and a loss of metabolic flexibility. *Oncogene* **30**, 1159–1173 (2011).
11. Yan, M. et al. The tumor suppressor folliculin regulates AMPK-dependent metabolic transformation. *J. Clin. Invest.* **124**, 2640–2650 (2014).
12. Tsun, Z. Y. et al. The Folliculin tumor suppressor is a GAP for the RagC/D GTPases that signal amino acid levels to mTORC1. *Mol. Cell* **52**, 495–505 (2013).
13. Petit, C. S., Roczniak-Ferguson, A. & Ferguson, S. M. Recruitment of folliculin to lysosomes supports the amino acid-dependent activation of Rag GTPases. *J. Cell Biol.* **202**, 1107–1122 (2013).
14. Fan, J. et al. Tyrosine phosphorylation of lactate dehydrogenase A is important for NADH/NAD$^+$ redox homeostasis in cancer cells. *Mol. Cell Biol.* **31**, 4938–4950 (2011).
15. Jin, L. et al. Phosphorylation-mediated activation of LDHA promotes cancer cell invasion and tumour metastasis. *Oncogene* **36**, 3797–3806 (2017).
16. Read, J. A., Winter, V. J., Eszes, C. M., Sessions, R. B. & Brady, R. L. Structural basis for altered activity of M- and H-isoenzyme forms of human lactate dehydrogenase. *Proteins* **43**, 175–185 (2001).
17. Yamamoto, S. & Storey, K. B. Dissociation–association of lactate dehydrogenase isozymes: influences on the formation of tetramers versus dimers of M4-LDH and H4-LDH. *Int. J. Biochem.* **20**, 1261–1265 (1988).
18. Zheng, Y., Guo, S., Guo, Z. & Wang, X. Effects of N-terminal deletion mutation on rabbit muscle lactate dehydrogenase. *Biochemistry (Mosc.)* **69**, 401–406 (2004).
19. Unkles, S. E. et al. Physiological and biochemical characterization of AnNitA, the *Aspergillus nidulans* high-affinity nitrite transporter. *Eukaryot. Cell* **10**, 1724–1732 (2011).
20. Yamamoto, S. & Storey, K. B. Dissociation–association of lactate dehydrogenase isozymes: influences on the formation of tetramers versus dimers of M4-LDH and H4-LDH. *Int. J. Biochem.* **20**, 1261–1265 (1988).
21. Valvona, C. J., Fillmore, H. L., Nunn, P. B. & Pilkington, G. J. The regulation and function of lactate dehydrogenase A: therapeutic potential in brain tumor. *Brain Pathol.* **26**, 3–17 (2016).
22. Tarmy, E. M. & Kaplan, N. O. Kinetics of *Escherichia coli* B D-lactate dehydrogenase and evidence for pyruvate-controlled change in conformation. *J. Biol. Chem.* **243**, 2587–2596 (1968).
23. Jiang, G. R., Nikolova, S. & Clark, D. P. Regulation of the *ldhA* gene, encoding the fermentative lactate dehydrogenase of *Escherichia coli*. *Microbiology* **147**, 2437–2446 (2001).
24. Yamamoto, S. & Storey, K. B. Influence of glycerol on the activity and tetramer–dimer state of lactate dehydrogenase isozymes. *Int. J. Biochem.* **20**, 1267–1271 (1988).
25. Boháčová, V., Dočolomanský, P., Breier, A., Gemeiner, P. & Ziegelhöffer, A. Interaction of lactate dehydrogenase with anthraquinone dyes: characterization of ligands for dye–ligand chromatography. *J. Chromatogr. B Biomed. Sci. Appl.* **715**, 273–281 (1998).
26. Cahn, R. D., Zwilling, E., Kaplan, N. O. & Levine, L. Nature and development of lactic dehydrogenases: the two major types of this enzyme form molecular hybrids which change in makeup during development. *Science* **136**, 962–969 (1962).
27. Shen, K. et al. Cryo-EM structure of the human FLCN-FNIP2–Rag–Ragulator complex. *Cell* **179**, 1319–1329 (2019).
28. Schopper, S. et al. Measuring protein structural changes on a proteome-wide scale using limited proteolysis-coupled mass spectrometry. *Nat. Protoc.* **12**, 2391–2410 (2017).
29. Woodford, M. R., Chen, V. Z., Backe, S. J., Bratslavsky, G. & Mollapour, M. Structural and functional regulation of lactate dehydrogenase-A in cancer. *Future Med. Chem.* **12**, 439–455 (2020).
30. el Hawrani, A. S., Moreton, K. M., Sessions, R. B., Clarke, A. R. & Holbrook, J. J. Engineering surface loops of proteins—a preferred strategy for obtaining new enzyme function. *Trends Biotechnol.* **12**, 207–211 (1994).
31. Clarke, A. R. et al. Site-directed mutagenesis reveals role of mobile arginine residue in lactate dehydrogenase catalysis. *Nature* **324**, 699–702 (1986).
32. Nookala, R. K. et al. Crystal structure of folliculin reveals a hidDENN function in genetically inherited renal cancer. *Open Biol.* **2**, 120071 (2012).
33. Nickerson, M. L. et al. Mutations in a novel gene lead to kidney tumors, lung wall defects, and benign tumors of the hair follicle in patients with the Birt–Hogg–Dubé syndrome. *Cancer Cell* **2**, 157–164 (2002).
34. Yang, Y. et al. The UOK 257 cell line: a novel model for studies of the human Birt–Hogg–Dubé gene pathway. *Cancer Genet. Cytogenet.* **180**, 100–109 (2008).
35. Linehan, W. M. et al. The metabolic basis of kidney cancer. *Cancer Discov.* **9**, 1006–1021 (2019).
36. Rai, G. et al. Pyrazole-based lactate dehydrogenase inhibitors with optimized cell activity and pharmacokinetic properties. *J. Med. Chem.* **63**, 10984–11011 (2020).
37. Paladino, A. et al. Chemical perturbation of oncogenic protein folding: from the prediction of locally unstable structures to the design of disruptors of Hsp90-client interactions. *Chemistry* **26**, 9459–9465 (2020).
38. Fosgerau, K. & Hoffmann, T. Peptide therapeutics: current status and future directions. *Drug Discov. Today* **20**, 122–128 (2015).
39. da Silva, N. F. et al. Analysis of the Birt–Hogg–Dubé (BHD) tumour suppressor gene in sporadic renal cell carcinoma and colorectal cancer. *J. Med. Genet.* **40**, 820–824 (2003).
40. Khoo, S. K. et al. Inactivation of BHD in sporadic renal tumors. *Cancer Res.* **63**, 4583–4587 (2003).
41. Kahnoski, K. et al. Alterations of the Birt–Hogg–Dubé gene (BHD) in sporadic colorectal tumours. *J. Med. Genet.* **40**, 511–515 (2003).
42. Nagy, A., Zoubakov, D., Stupar, Z. & Kovacs, G. Lack of mutation of the folliculin gene in sporadic chromophobe renal cell carcinoma and renal oncocytoma. *Int. J. Cancer* **109**, 472–475 (2004).
43. Gad, S. et al. Mutations in *BHD* and *TP53* genes, but not in *HNF1β* gene, in a large series of sporadic chromophobe renal cell carcinoma. *Br. J. Cancer* **96**, 336–340 (2007).
44. Rai, G. et al. Discovery and optimization of potent, cell-active pyrazole-based inhibitors of lactate dehydrogenase (LDH). *J. Med. Chem.* **60**, 9184–9204 (2017).

Methods

Mass spectrometry. FLCN was immunoprecipitated from whole-cell lysate, subjected to SDS–PAGE and stained with Imperial Protein Stain (Thermo Fisher). Visible bands were digested in-gel with trypsin overnight at 37 °C, following reduction with DTT and alkylation with iodoacetamide. Mass spectrometry was performed at the Weill Cornell Medicine (WCM) Meyer Cancer Center Proteomics & Metabolomics Core Facility as described in previously published work[45]. The digests were vacuum-centrifuged to near dryness and desalted by C18 stage tips. A Thermo Fisher Scientific EASY-nLC 1000 system coupled online to a Fusion Lumos mass spectrometer (Thermo Fisher Scientific) was used. Buffer A (0.1% formic acid in water) and buffer B (0.1% FA in 100% acetonitrile (ACN)) were used as mobile phases for gradient separation. A 75 µm × 20 cm column (ReproSil-Pur C18-AQ, 3 µm, Dr. Maisch) was packed in house for peptide separation. Peptides were separated with a gradient of 3–32% buffer B over 50 min and 32–80% B over 10 min at a flow rate of 300 nl min^{-1}. The Fusion Lumos mass spectrometer was operated in data-dependent mode. Full MS scans were acquired in an Orbitrap mass analyzer over a range of 300–1,500 *m*/*z* with a resolution of 60,000 at *m*/*z* 200. The top 15 most abundant precursors with charge states between 2 and 6 were selected with an isolation window of 1.4 thomsons and fragmented by higher-energy collisional dissociation with a normalized collision energy of 35. MS/MS scans were acquired in an Orbitrap mass analyzer with resolution of 15,000 at *m*/*z* 200. The automatic gain control target value was 1e6 for full scans and 5e4 for MS/MS scans, respectively, and the maximum ion injection time was 50 ms for both. The raw files were processed using the MaxQuant[46] computational proteomics platform version 1.5.5.1 (Max Planck Institute) for protein identification. The fragmentation spectra were used to search the UniProt human protein database (downloaded 21 September 2017). Oxidation of methionine and protein N-terminal acetylation were used as variable modifications for database searching. The precursor and fragment mass tolerances were set to 7 and 20 ppm, respectively. Both peptide and protein identifications were filtered at a 1% false discovery rate based on a decoy search using a database with the protein sequences reversed.

Limited proteolysis mass spectrometry. Limited proteolysis was achieved by exposing recombinant LDHA (10 ng µl^{-1}) ± FLCN-10 peptide (10 µM) to 20 µg ml^{-1} trypsin in 25 mM ammonium bicarbonate solution. At intervals of 5, 10, 15, 30 and 60 min, 30 µl of the combined protein/trypsin solution was transferred to a second tube with 6 µl of SDS gel buffer and then boiled. The resulting partially proteolyzed mixture was then run on an SDS–PAGE gel and stained with Coomassie Brilliant Blue. The selected protein gel bands were excised and in-gel-digested with trypsin (0.6 µg) and the tryptic peptides were subjected to MALDI-MS on an in-house ABSCIEX TOF/TOF 5800 mass spectrometer. Positive-mode time of flight was used to identify peptides, and individual peptides were sequenced by MS/MS. All sequence and peptide fingerprint data were searched using the UniProt database and Mascot search engine.

Mammalian cell culture. HAP1 cell lines were obtained from Horizon Discovery. UOK257 and UOK257-2 cell lines were provided by LSS. All other cell lines were obtained from the ATCC. Catalog numbers are listed in Supplementary Table 3. Cells were cultured at 37 °C in a CellQ incubator at 5% CO_2. HEK293, Du145, J82, UMUC-3, MDA-MB-231, A549, UOK257 and UOK257-2 cells were grown in DMEM (Sigma-Aldrich), 786-O, PC3, SW780, LNCaP and H1299 cells in RPMI-1640 (Sigma-Aldrich), A498 cells in minimum essential medium (MEM; Sigma-Aldrich), Caki-1, Caki-2, HT29, T24 and RT4 cells in McCoy's 5A medium (Sigma-Aldrich) and HAP1 cells in Isocove's modified Dulbecco's medium (IMDM; Gibco). Cell lines were tested for mycoplasma contamination at the early stages of the experiments.

Plasmids and transient transfection. Cultured cells were transiently transfected using TransIT-2020 (Mirus Bio) transfection reagent according to the manufacturer's protocol, incubated at 37 °C for 24 h (HEK293) or 48 h (UOK257, ccRCC cell lines) and subsequently prepared for protein extraction (next section). Control short interfering RNA (siRNA) or FLCN ON-TARGETplus siRNA (Dharmacon) (50 µM) was transiently transfected in LDHA knockout (KO) or LDHB KO HAP1 cells for 48 h using TransIT-2020. All mammalian expression experiments used genes cloned into the pcDNA3 vector backbone (Thermo Fisher). LDHA/LDHB chimeric constructs were synthesized by GeneWiz and subcloned into pcDNA3 (Thermo Fisher). Information about the DNA primer and siRNA sequences is provided in Supplementary Table 3.

Protein extraction, immunoprecipitation, pulldown and immunoblotting. Protein extraction from mammalian cells was carried out using methods as previously described[47]. Tissues were homogenized with acid-washed glass beads and a mini-Beadbeater 8 cell disruptor (Biospec Products). Samples were agitated for 30 s at maximum speed followed by a 30-s incubation on ice. This procedure was repeated six times followed by a 10,000*g*, 5-min centrifugation to pellet the beads and unbroken cells. The supernatant was transferred to a new microtube and centrifuged (10,000*g*, 10 min) to pellet insoluble aggregates. The supernatant was then transferred to a fresh microtube. For IP, mammalian cell lysates were incubated with anti-FLAG or anti-HA antibody-conjugated agarose beads (Sigma) for 2 h at 4 °C or with anti-LDHA or anti-FLCN antibody for 1 h followed by protein G agarose for 2 h at 4 °C. For biotinylated peptide pulldown, lysates were incubated with biotinylated peptide for 1 h at 4 °C, followed by incubation with streptavidin agarose for 1 h at 4 °C. For Cibacron Blue pulldown, mammalian cell lysates were incubated with Cibacron Blue agarose for 1 h at 4 °C. Immunopellets were washed four times with fresh lysis buffer (20 mM Tris-HCl pH 7.4, 100 mM NaCl, 1 mM $MgCl_2$, 0.1% NP40, cOmplete protease inhibitor cocktail (Millipore-Sigma) and PhosSTOP (Millipore-Sigma)) and eluted in 5× Laemmli buffer. Precipitated proteins were separated by SDS–PAGE and transferred to nitrocellulose membranes. Co-immunoprecipitated proteins were detected by immunoblotting with primary antibodies (anti-FLAG (Sigma), anti-GAPDH (1D4, Enzo Life Sciences), anti-LDHA (E-9, abcam), anti-HA (C29F4), anti-FLCN (D14G9), anti-LDHB, anti-phospho-Tyr10-LDHA, anti-cleaved caspase-3 (Asp175) (5A1E, Cell Signaling)) followed by secondary antibodies raised against mouse, rabbit and rat (Cell Signaling) at 1:4,000 dilution. Densitometry was performed using Image Studio Lite (LI-COR Biosciences). The catalog numbers of the commercially available antibodies used are provided in Supplementary Table 3.

Native polyacrylamide gel electrophoresis. Proteins were extracted as above. The following 5× sample loading buffer was prepared: 250 mM Tris-HCl, pH 6.8, 30% glycerol, 0.05% bromophenol blue. Samples were incubated with sample buffer for 5 min at room temperature and loaded on a prepared Criterion Tris-HCl protein gel (Bio-Rad) in 1× native running buffer (25 mM Tris base, 192 mM glycine). Proteins were subjected to electrophoresis at 100 V for 2 h and transferred to a nitrocellulose membrane with an Ready-to-Assemble (RTA) transfer kit according to the manufacturer's protocol (Bio-Rad) using the standard 30-min transfer protocol on a TransBlot Turbo system (Bio-Rad).

LDH activity assay. LDH activity was measured according to the manufacturer's protocol (MAK066, Sigma-Aldrich). In brief, 25 ng of recombinant LDHA was pre-incubated with either peptide or recombinant FLCN protein for 30 min on ice. Samples were then transferred to an optically clear 96-well plate and substrate mix was added to each well. Absorbance was measured at 450 nm every 5 min until saturation. For measurement of LDH activity in lysates, 1 µg of whole-cell lysate was diluted into 50 µl total volume with 1× assay buffer (included in MAK066) in a 96-well plate. Absorbance at 450 nm was measured every 5 min following addition of substrate mix. All experiments were performed using three biological replicates and measured in triplicate.

LDHA kinetics and inhibition assay. The effect of FLCN, FLCN-10 peptide and FX11 (small-molecule inhibitor of LDHA control) on LDHA activity has been examined in previously published reactions[48,49]. The reaction contains 50 mM Tris-HCl buffer pH 7.0, 2 mM pyruvate, varied concentrations of NADH and 2 nM FLCN or 100 nM FLCN-10 peptide, or 60 µM FX11. All assays were carried out in triplicate, and at least two independent assays were performed. GraphPad Prism 6 was used to calculate half-maximum inhibitory concentrations (IC_{50}). Microsoft Excel was used to calculate kinetic parameters with appropriate nonlinear regression models, including Michaelis–Mention and allosteric sigmoidal models for substrates and cofactors. Only reaction data in the linear range were used in computations, which typically occurred within a reaction time of 5 min. The inhibitor constants (K_i) for FLCN, FLCN-10 peptide and FX11 were calculated using the Lineweaver–Burk plot and a web-based tool (https://bioinfo-abcc.ncifcrf.gov/IC50_Ki_Converter/index.php) for converting IC_{50} values to K_i values for inhibitors of enzyme activity and ligand binding[50].

Protein purification. FLCN and LDHA were cloned into pRSET-A (Thermo Fisher) and expressed and purified from *Escherichia coli* strain BL21 (DE3). Transformed cells were grown at 37 °C in LB medium with 50 mg l^{-1} ampicillin until the optical density at 600 nm reached 0.6. The cultures were then cooled to 30 °C, induced with 1 mM IPTG and grown overnight. Cells were collected by centrifugation and lysed by sonication in fresh lysis buffer without detergent (20 mM Tris-HCl pH 7.4, 100 mM NaCl, 1 mM $MgCl_2$, protease inhibitor cocktail (Millipore-Sigma) and PhosSTOP (Millipore-Sigma)). After sonication, Triton X-100 was added to a final concentration of 1% before pelleting insoluble debris by centrifugation. The supernatant was collected, and expression was assessed by immunoblotting. Isolation was accomplished by two sequential Ni-NTA agarose (Qiagen) pulldowns. The lysate was incubated with Ni-NTA agarose (Qiagen) for 2 h at 4 °C. Proteins bound to Ni-NTA agarose were washed three times with lysis buffer (as above) followed by two washes with 50 mM imidazole in lysis buffer. Proteins were then eluted in 500 mM imidazole in lysis buffer and concentrated in 10K Amicon Ultra centrifugal filters (Millipore). Concentrations were determined using the Micro BCA protein assay kit (Thermo Scientific) according to the manual protocol. Purified protein was run on an SDS–PAGE gel and Coomassie-stained to confirm purity before use in assays.

Ex vivo peptide treatment. Tumor and adjacent normal renal tissue from the patient with BHD were obtained with written informed consent on an Institutional Review Board (IRB)-approved protocol from the Department of Urology at SUNY Upstate Medical University. This procedure was compliant with all relevant ethical

regulations. At the time of partial nephrectomy, which was done with <15 min of renal ischemia, BHD tumors were dissected into 3- to 5-mm^3 pieces and cultured on a presoaked gelatin sponge (Johnson & Johnson) in 24-well plates containing 2 ml of RPMI-1640 with 10% FBS and antibiotic/antimycotic solution. Tissues were cultured at 37 °C for 16 h, followed by addition of the indicated concentrations of FLCN-10–Rhod-B and further incubation at 37 °C for 2 h. Following treatment, tissues were either homogenized and lysed for immunoblotting (as above) or fixed in 10% formalin and embedded in paraffin. Thin sections were mounted on slides and stained with H&E or alternately with anti-FLCN and anti-LDHA for immunofluorescence (next section).

Fluorescence microscopy. For peptide treatments, HEK293 cells were seeded on glass coverslips and grown overnight. The following day, cells were treated with rhodamine B-labeled peptide for 2 h, followed by fixation in 1% paraformaldehyde for 5 min, and mounted on slides using Prolong Gold Anti-fade reagent with 4′,6-diamidino-2-phenylindole (DAPI, Thermo Fisher). Images were obtained using a Leica SP8 Confocal Microscope using the LAS X software platform. Cells or thin tissue sections were fixed in 2% paraformaldehyde, permeabilized in 0.2% Triton X-100, and blocked for 2 h in 1% BSA at room temperature before staining. After three washes in 1× phosphate-buffered saline, slides were incubated with primary antibodies to LDHA (sc-137243, Santa Cruz, 1:50) and FLCN (NBP1-44995, Novus Biologicals, 1:30) overnight at 4 °C. Following several washes in 1× phosphate-buffered saline, tissues were incubated with secondary antibodies Alexa Fluor 594 and Alexa Fluor 488 (Life Technologies) diluted in 1% BSA for 45 min at room temperature. Nuclear staining was achieved using ProLong Gold antifade reagent with DAPI (Life Technologies). Representative images were captured on a Zeiss LSM710 confocal microscope.

Binding measurements. LDHA at the indicated concentrations was incubated on ice in 50 mM Tris pH 7.2, 150 mM NaCl, 1 mM tris(2-carboxyethyl)phosphine (TCEP), 4 mM $MgCl_2$ with 1 mM rhodamine B-labeled FLCN peptide for 30 min. Fluorescence anisotropy was measured in triplicate using a SpectraMax i3 system equipped with a rhodamine fluorescence polarization module (l_{ex}/l_{em}, 535 nm/595 nm). Curve fitting was carried out in KaleidaGraph 4.0.

Seahorse metabolic assay. UOK cells were transfected in 100-mm dishes at 50% confluency and incubated for 24 h. Subsequently, cells were seeded at 1×10^5 per well 24 h before assay initiation in a 96-well plate, and treated for the indicated times immediately preceding measurements. A glycolytic stress test was then carried out on an Agilent Seahorse XF instrument according to the manufacturer's protocol.

Flow cytometric analysis. Fluorescence-activated cell sorting (FACS) analysis was performed according to the protocol in the Annexin V:FITC kit (Bio-Rad). In brief, cells were plated at 0.5×10^6 and incubated at 37 °C for 16 h. Cells were subsequently treated with FLCN-10 peptide at the indicated concentrations for 1–2 h. Cells were trypsinized, collected and washed once with 1× binding buffer (included in the kit). Annexin V-FITC was added at 1:40 and incubated for 10 min at room temperature in the dark. Following one wash with 1× binding buffer, propidium iodide was added, then the cells were immediately run on a Becton Dickinson LSRFortessa instrument (BD Biosciences). Data were analyzed using FlowJo software v10.6.2 (Becton Dickinson).

Linear peptide synthesis. Linear peptides (Fig. 2b) were synthesized and HPLC-purified to >95% purity by Life Technologies.

General procedures for peptide synthesis. *Resin loading.* Resin (0.5 mmol g^{-1} loading) was swollen in CH_2Cl_2 for 30 min then washed with dimethylformamide (DMF; 3 × 3 ml). A solution of entering Fmoc-amino acid, *N*,*N*′-diisopropylcarbodiimide (DIC) and oxyme (5:5, 5 equiv. over resin loading) and 5% 4-dimethylaminopyridine (DMAP) in DMF (3 ml) was added and the resin shaken at room temperature for 4 h. The resin was washed with DMF (2 × 3 ml) and capping was performed by treatment with acetic anhydrid e/*N*,*N*-diisopropylethylamine (DIEA) in DCM (1 × 30 m). The resin was then washed with DMF (2 × 3 ml), CH_2Cl_2 (2 × 3 ml) and DMF (2 × 3 ml). The resin was subsequently submitted to fully automated iterative peptide assembly solid-phase peptide synthesis (Fmoc-SPPS).

Peptide assembly via iterative fully automated microwave-assisted SPPS. Peptides were assembled by stepwise microwave-assisted Fmoc-SPPS on a Biotage Alstra Initiator+ peptide synthesizer, operating in a 0.1 mmol scale. Activation of entering Fmoc-protected amino acids (0.3 M solution in DMF) was performed using 0.5 M ethyl cyanohydroxyiminoacetate (Oxyma, Sigma-Aldrich) in DMF/0.5 M DIC in DMF (1:1:1 molar ratio), with a 5 equiv. excess over the initial resin loading. Coupling steps were performed for 7 min at 75 °C. Fmoc-deprotection steps were performed by treatment with a 20% piperidine solution in DMF at room temperature (1 × 10 m). Following each coupling or deprotection step, peptidyl-resin was washed with DMF (4 × 3.5 ml). Upon complete chain assembly, the resin was washed with DCM (5 × 3.5 ml) and gently dried under a nitrogen flow.

Cleavage from the resin. Resin-bound peptide was treated with a mixture of ice-cold trifluoroacetic acid (TFA), triisopropylsilane (TIS), water and thioanisole (90:5:2.5:2.5 vol/vol/vol/vol, 4 ml). After gently shaking the resin for 2 h at room temperature, the resin was filtered and washed with neat TFA (2 × 4 ml). The combined cleavage solutions were worked up as indicated in the next section.

Work-up and purification. The cleavage mixture was concentrated under a nitrogen stream and then added dropwise to ice-cold diethyl ether (40 ml) to precipitate the crude peptide. The crude peptide was collected by centrifugation and washed with further cold diethyl ether to remove scavengers. Residual diethyl ether was removed by a gentle nitrogen flow and the crude peptide was purified by reverse-phase (RP)-HPLC and lyophilized.

Peptide cyclization. Peptides for head-to-tail cyclization were detached from the resin using 25% 1,1,1,3,3,3-hexafluoro-2-propanol (HFP) in DCM (4 × 10 ml). Collected fractions were combined and dried under reduced pressure. The residue was then dissolved in dry DMF (1.25 mM) and hexafluorophosphate benzotriazole tetramethyl uronium/*N*,*N*-diisopropylethylamine (HBTU/DIEA) were added (1.1 and 2 equiv. respectively). The reaction was left overnight and then DMF evaporated. The dry residue was then treated with standard TFA-based cleavage solution to yield the fully unprotected, cyclic peptides.

Synthesis of fluorescein-labeled peptides. Cysteine-bearing peptides were conjugated to bifunctional fluorescein-maleimide, 6-isomer (MAL-FAM), (Lumiprobe) as follows. Peptide (1 equiv.) was first dissolved in phosphate buffer (Na_2HPO_4 0.4 M, pH 7.8). The resulting solution was ice-cooled and mixed with MAL-FAM solution (1.2 equiv., 50:50 acetonitrile/water mixture). The reaction mixture was left to react under gentle shaking until full conversion of the reagents (monitored by RP-HPLC). At reaction completion, the conjugation products were isolated by preparative RP-HPLC and lyophilized.

Reverse-phase high-performance liquid chromatography analysis and purification. Analytical RP-HPLC was performed on a Shimadzu Prominence HPLC instrument (Shimadzu) using a Shimadzu Shimpack GWS C18 column (5 µm, 4.6 mm inner diameter (i.d.) × 150 mm). Analytes were eluted using a binary gradient of mobile phase A (100% water, 0.1% TFA) and mobile phase B (30% water, 70% acetonitrile, 0.1% TFA) using the following chromatographic method: 10% B to 100% B in 14 min; flow rate, 1 ml min^{-1}. Preparative RP-HPLC was performed on a Shimadzu HPLC system using a Shimadzu C18 column (10 µm, 21.2-mm (i.d.) × 250 mm) using the following chromatographic method: 0% B to 100% B in 45 min; flow rate, 14 ml min^{-1}. Pure RP-HPLC fractions (>95%) were combined and lyophilized.

Electro-spray ionization mass spectrometry. Electro-spray ionization mass spectrometry was performed using a Bruker Esquire 3000+ instrument equipped with an electro-spray ionization source and a quadrupole ion trap detector (QITD).

Quantification, statistical analysis and reproducibility. The data presented are representative of three biological replicates, unless otherwise specified. All statistics were performed using GraphPad Prism version 7.00 for Windows (GraphPad Software, https://www.graphpad.com). Statistical significance was ascertained between individual samples using a parametric unpaired *t*-test. Significance is denoted by asterisks in each figure: $*P < 0.05$; $**P < 0.01$; $***P < 0.001$; $****P < 0.0001$. Error bars represent the standard deviation for three independent experiments, unless otherwise indicated.

No statistical methods or criteria were used to include or exclude samples. All immunoblots and microscopy in Figs. 1b,c, 3c, 4a–c, 5b–d and 6a,b and Extended Data Figs. 1b,c, 2a–c,e, 3c, 5a–d, 6g, 7a–d, 8a and 9a,b,e,f were repeated at least twice independently, with similar results.

Reporting Summary. Further information on research design is available in the Nature Research Reporting Summary linked to this Article.

Data availability

The MS proteomics data have been deposited to the ProteomeXchange Consortium via the PRIDE[51] partner repository with the dataset identifier PXD018410 (www.ebi.ac.uk/pride/). Source data are provided with this paper.

References

45. Wang, Y. et al. Fascin inhibitor increases intratumoral dendritic cell activation and anti-cancer immunity. *Cell Rep.* **35**, 108948 (2021).
46. Cox, J. & Mann, M. MaxQuant enables high peptide identification rates, individualized p.p.b.-range mass accuracies and proteome-wide protein quantification. *Nat. Biotechnol.* **26**, 1367–1372 (2008).
47. Woodford, M. R. et al. The FNIP co-chaperones decelerate the Hsp90 chaperone cycle and enhance drug binding. *Nat. Commun.* **7**, 12037 (2016).
48. Gay, R. J., McComb, R. B. & Bowers, G. N. Jr Optimum reaction conditions for human lactate dehydrogenase isoenzymes as they affect total lactate dehydrogenase activity. *Clin. Chem.* **14**, 740–753 (1968).

49. Powers, J. L., Kiesman, N. E., Tran, C. M., Brown, J. H. & Bevilacqua, V. L. H. Lactate dehydrogenase kinetics and inhibition using a microplate reader. *Biochem. Mol. Biol. Educ.* **35**, 287–292 (2007).
50. Cer, R. Z., Mudunuri, U., Stephens, R. & Lebeda, F. J. IC_{50}-to-K_i: a web-based tool for converting IC_{50} to K_i values for inhibitors of enzyme activity and ligand binding. *Nucleic Acids Res.* **37**, W441–W445 (2009).
51. Vizcaino, J. A. et al. 2016 update of the PRIDE database and its related tools. *Nucleic Acids Res.* **44**, D447–D456 (2016).

Acknowledgements

We thank B. A. Knutson, R. A. Oot, S. Wilkens and L. Neckers for assistance and scientific discussions as well as D. E. Post of the Upstate Cancer Center Biorepository. This work was partly supported with federal funds from the Frederick National Laboratory for Cancer Research, National Institutes of Health, under contract no. HHSN26120080001E (L.S.S.) and with funds from SUNY Upstate Medical University, Upstate Cancer Center and the Upstate Foundation (M.M.).

Author contributions

M.R.W., A.J.B.-W., R.A.S., S.J.B., A.R.B., F.H., P.K., A.G., D.R.L., M.C., S.A.S., S.M.J., A.B. and M.M. performed experiments. M.R.W., A.J.B.-W., G.C., T.A.H., W.G.S.-S., S.N.L., L.S.S., W.M.L., A.B., D.B., G.B. and M.M. designed experiments. M.R.W., R.A.S., A.B., D.B., G.B. and M.M. wrote the manuscript. M.R.W. and M.M. conceived the project.

Competing interests

The authors declare no competing interests.

Additional information

Extended data is available for this paper at https://doi.org/10.1038/s41594-021-00633-2.

Supplementary information The online version contains supplementary material available at https://doi.org/10.1038/s41594-021-00633-2.

Correspondence and requests for materials should be addressed to G.B. or M.M.

Peer review information *Nature Structural & Molecular Biology* thanks Filippo Minutolo and the other, anonymous, reviewer(s) for their contribution to the peer review of this work.

Reprints and permissions information is available at www.nature.com/reprints.

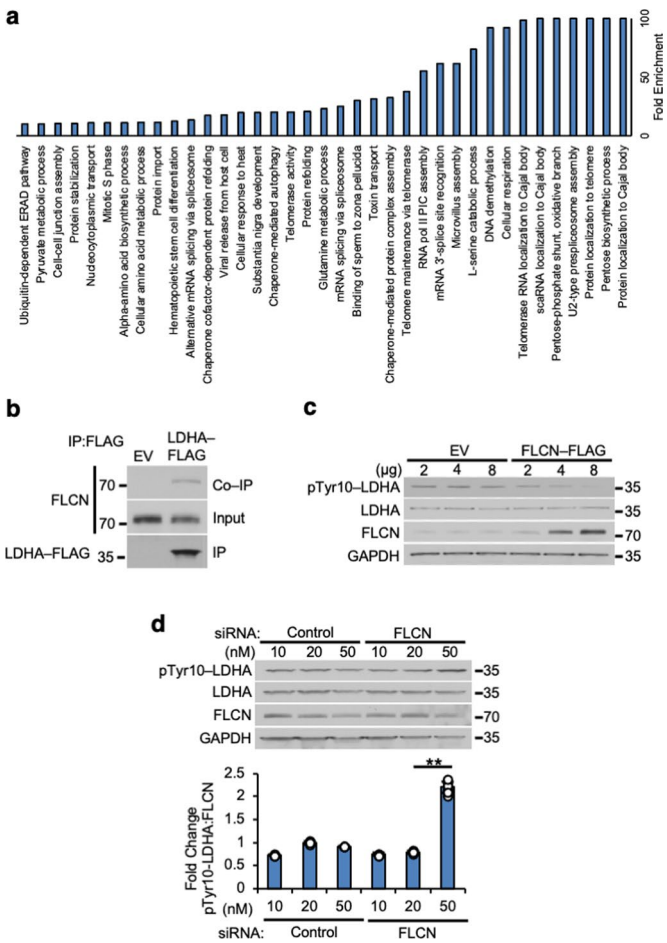

Extended Data Fig. 1 | The tumor suppressor FLCN mediated binding and inhibition of LDHA. a) Gene Ontology term analysis of FLCN proteomic data using Panther v15.0 (pantherdb.org). **b**) LDHA-FLAG IP from HEK293 cells immunoblotted with anti-FLCN antibody. **c**) Titration of FLCN-FLAG expression in HEK293 cells immunoblotted with anti-pTyr10-LDHA antibody. **d**) Titration of siRNA targeting FLCN in HEK293 cells immunoblotted with anti-pTyr10-LDHA antibody. Bar chart contains densitometry of pTyr10-LDHA:FLCN ratio. Unpaired Student's *t*-test, ($p < 2.9\text{x}10^{-10}$, n=3). Data shown as mean ± s.d.

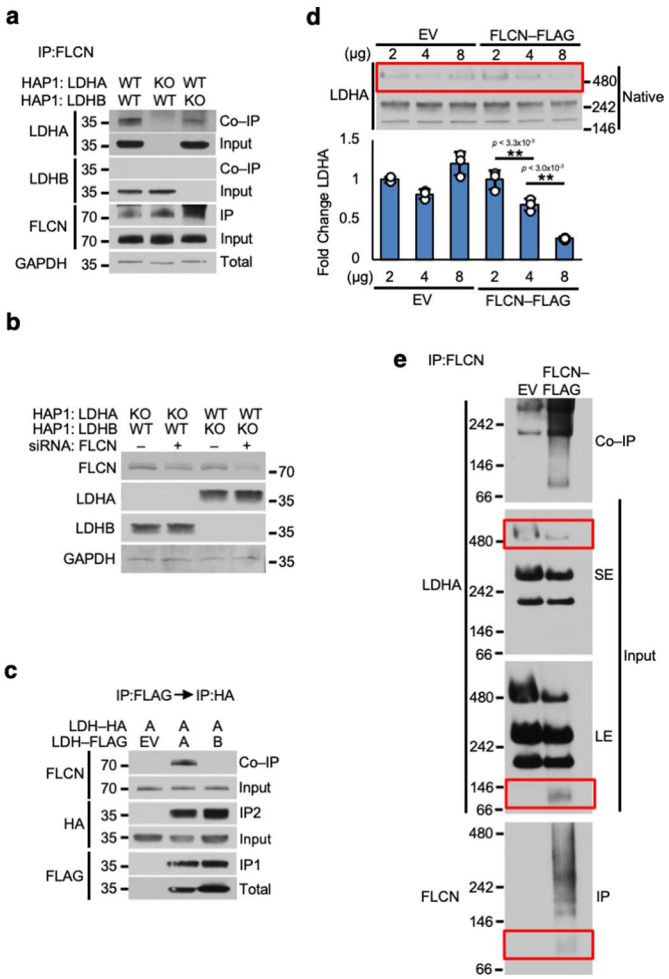

Extended Data Fig. 2 | Inherent specificity of FLCN for binding to dimeric LDHA. a) IP of endogenous FLCN from whole cell lysates of LDHA or LDHB knockout HAP1 cells. Immunoblotted with anti-FLCN antibody. **b**) Western blot of siRNA knockdown of FLCN in Fig. 1d. **c**) Tagged LDHA and LDHB subunits were consecutively immunoprecipitated and immunoblotted with anti-FLCN. **d**) Lysates from Extended Data Fig. 1c subjected to Native PAGE. Bar chart contains ratio of densitometry of largest LDHA oligomer:GAPDH (see Extended Data Fig. 1c; Unpaired Student's *t*-test, n=3). Data shown as mean ± s.d. **e**) IP of FLCN from HEK293 cells subjected to Native PAGE. SE = short exposure of immunoblot, LE = long exposure of immunoblot.

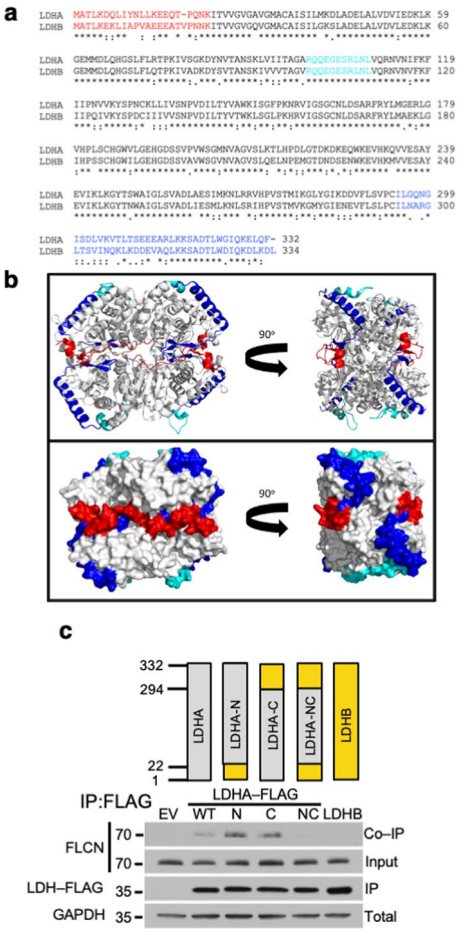

Extended Data Fig. 3 | The tumor suppressor FLCN specifically binds to the amino and carboxy domain of LDHA. a) Sequence alignment of human LDHA and human LDHB using https://clustalw.ddbj.nig.ac.jp/. The red N- and blue C-terminal residues that were swapped to generate the N, C and NC chimeric constructs used in Extended Data Fig. 2c are highlighted. The active site loop (99–110) is colored cyan. **b**) LDHA tetramer (PDB ID: 1i10) in ribbon (top) and surface (bottom) models represented in the standard view (left) and 90° rotated view (right). The N-terminus (residues 1–22) is highlighted in red and the C-terminus (residues 294–332) is highlighted in blue. Note the proximity of the C-terminal helix (blue) to the active site loop (residues 99–110; cyan) within each subunit. In the tetrameric arrangement, the N- and C-terminal residues of adjacent subunits form a continuous surface. Structure rendered using PyMOL 2.3. **c**) LDHA/LDHB chimeric constructs were transfected into HEK293 cells and immunoprecipitated. Co-IP of FLCN was detected by immunoblot.

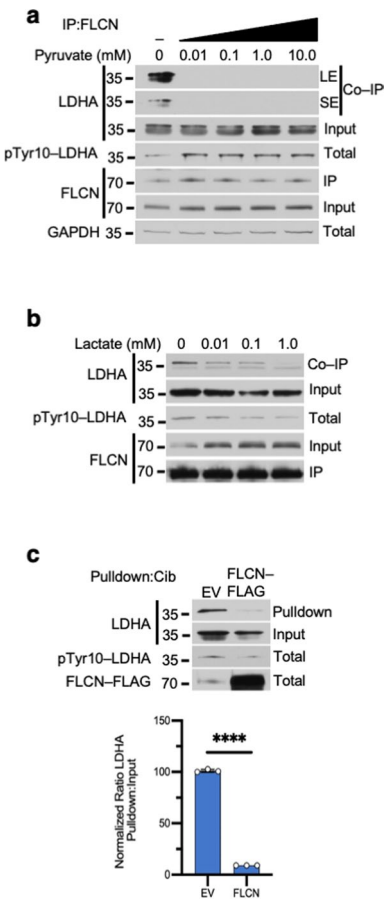

Extended Data Fig. 4 | FLCN interference with cofactor binding to LDHA. a) Immunoblot of anti-FLCN IPs and whole cell extracts following exogenous addition of pyruvate to HEK293s (6 h treatment duration; n=3). SE = short exposure of immunoblot, LE = long exposure of immunoblot. **b**) Immunoblot of anti-FLCN IPs and whole cell extracts following exogenous addition of lactate to HEK293s (6 h treatment durations; n=3). **c**) Pulldown of LDHA from cell lysate expressing EV or FLCN-FLAG using Cibacron blue agarose was evaluated by immunoblot. Bar chart represents the ratio of Pulldown:Input normalized to EV. Unpaired Student's t-test, ($p < 3.3x10-8$; n=3). Data shown as mean ± s.d.

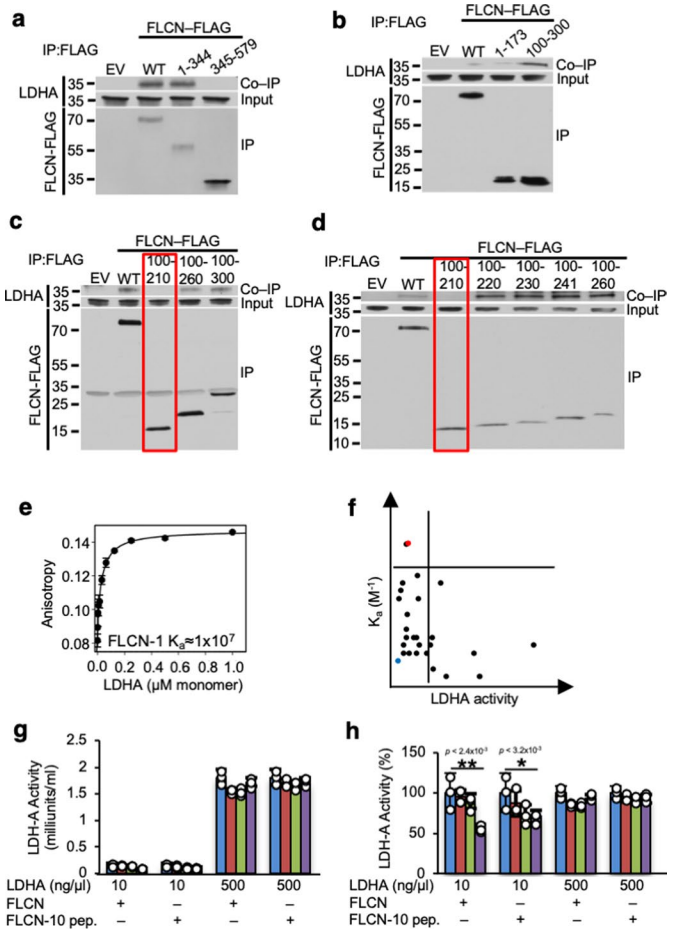

Extended Data Fig. 5 | FLCN-10 peptide is able to effectively inhibit dimeric but not tetrameric LDHA. a–**d**) Immunoprecipitation of transiently expressed short segments of FLCN-FLAG protein implies the critical interacting region with LDHA. **e**) Ka of LDHA with FLCN-1 peptide (See Fig. 2c), measured by fluorescence polarization anisotropy (n=3). **f**) Ka plotted against LDHA activity in the presence of peptides. FLCN-1 peptide (blue) and FLCN-10 peptide (red) are highlighted. **g**) LDHA activity at 10 ng/μl (predominantly dimeric) and 500 ng/μl (predominantly tetrameric) in the presence of increasing amounts of recombinant FLCN protein or FLCN-10 peptide (n=3). Data shown as mean ± s.d. **h**) Data from Extended Data Fig. 5g presented as percent activity. Unpaired Student's t-test, n=3. Data shown as mean ± s.d.

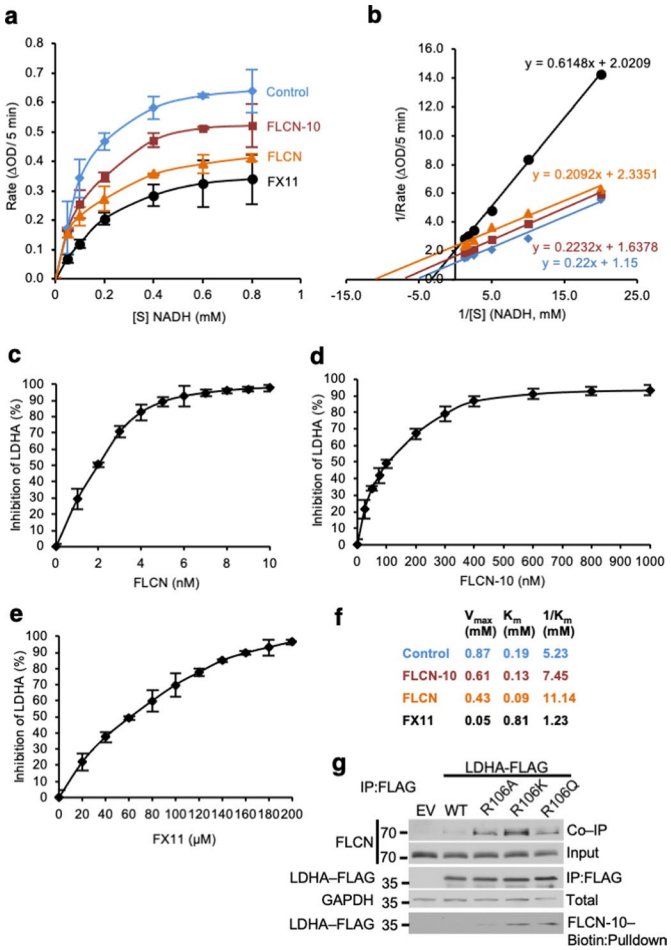

Extended Data Fig. 6 | FLCN-10 peptide uncompetitively inhibits LDHA. a) Michaelis-Menten kinetics of LDHA in the presence of FLCN protein, FLCN-10 peptide, or FX11 (n=3). Data shown as mean ± s.d. **b**) FLCN-10 is an uncompetitive inhibitor of LDHA based on Lineweaver-Burke plot (n=3). **c**–**e**) IC_{50} measurements for LDHA in the presence of FLCN protein, FLCN-10 peptide, or FX-11 (n=3). Data shown as mean ± s.d. **f**) Summary of LDHA enzyme kinetics. **g**) LDHA-R106-FLAG mutants were transiently transfected and immunoprecipitated from HEK293 cells. FLCN interaction assessed by immunoblotting. Binding to FLCN-10-Biotin peptide was assessed by Streptavidin pulldown.

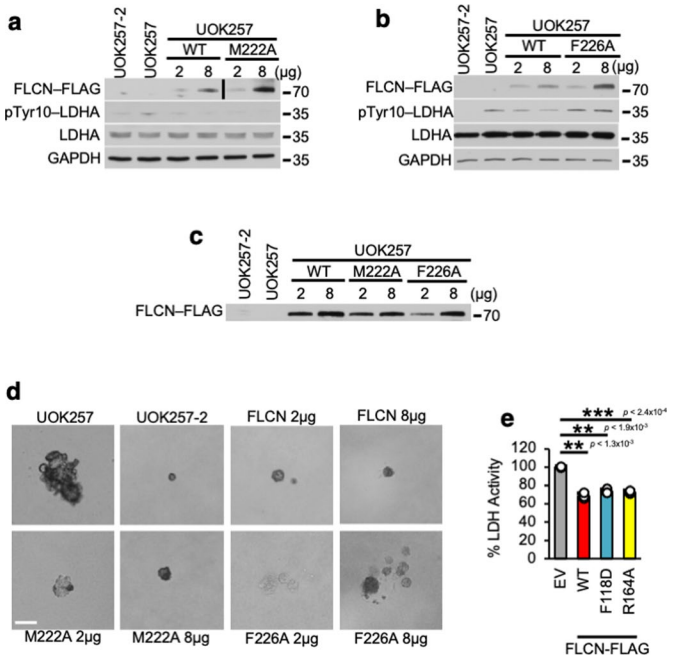

Extended Data Fig. 7 | inhibitory function of FLCN toward LDHA and its physiological outcome. a) Western blot confirming transfection of FLCN-WT-FLAG and FLCN-M222A-FLAG or **b**) FLCN-WT-FLAG and FLCN-F226A-FLAG in UOK257 cells in Fig. 3d. **c**) Western blot confirming transfection of FLCN-WT-FLAG, FLCN-M222A-FLAG, or FLCN-F226A-FLAG in Fig. 3f. **d**) Representative images of UOK257 colonies in soft agar from Fig. 3f. Scale bar = 100 μM. **e**) LDHA activity in UOK257 cells transfected with EV, WT FLCN, FLCN-F118D-FLAG and FLCN-R164A-FLAG. Unpaired Student's t-test, n=3. Data shown as mean ± s.d. *P < 0.05, **P < 0.005, ***P < 0.001.

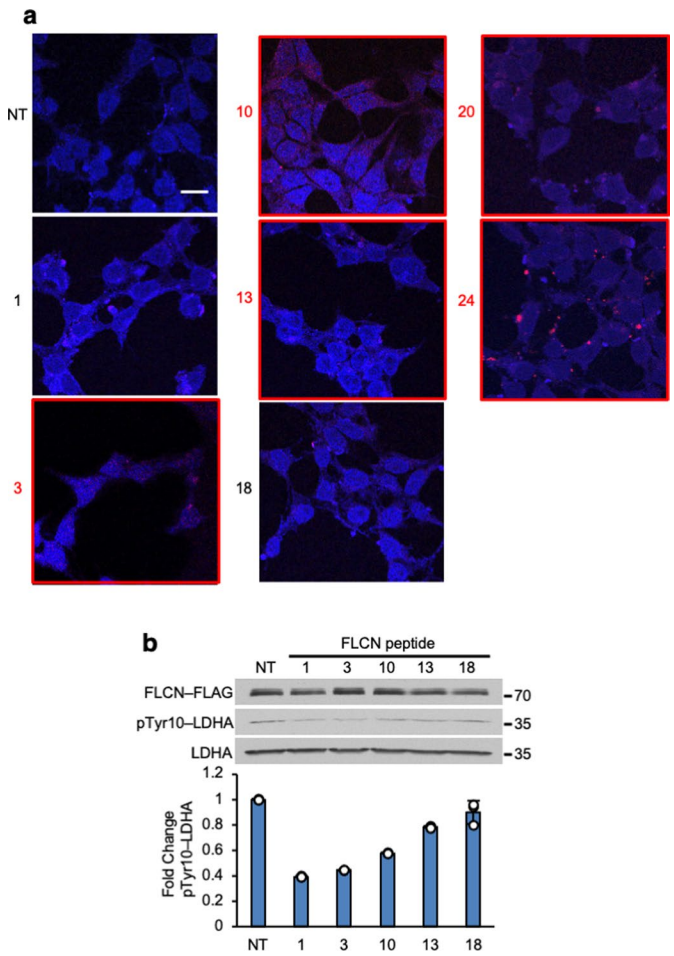

Extended Data Fig. 8 | FLCN-10 peptide is cell-permeable and inhibits LDHA. a) Fluorescence microscopy of HEK293 cells treated with 1 μM Rhodamine B-labeled peptides from Fig. 2b. Peptides that are resident after two hours treatment have been denoted with a red number and box. NT = No treatment. Scale bar = 10 μM. **b**) HEK293 cells treated with peptides from Extended Data Fig. 8a. Bar chart represents fold change of pTyr10-LDHA normalized to NT. Data shown as mean ± s.d. (n=3).

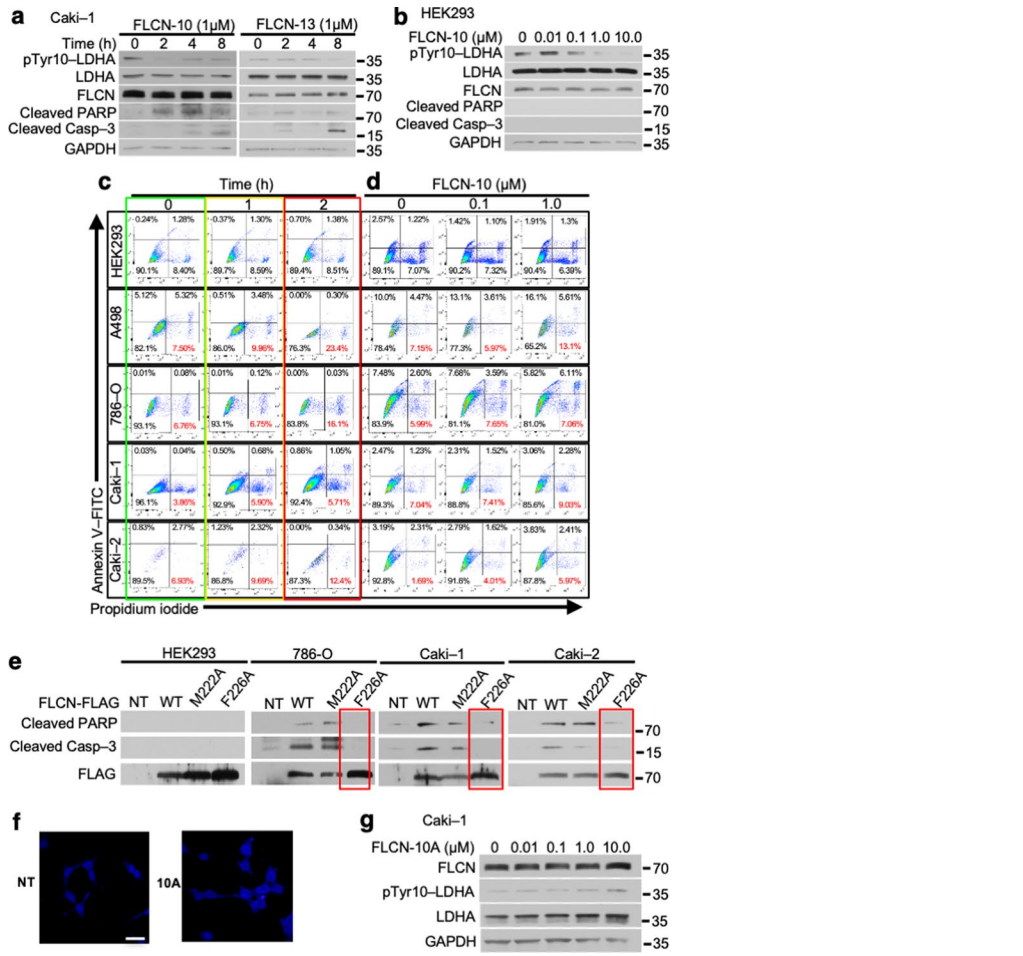

Extended Data Fig. 9 | FLCN-10 peptide inhibits LDHA activity and induces cell death in ccRCC cell lines. a) Caki-1 cells treated for 2 h with FLCN-10 or FLCN-13 were blotted using anti-cleaved caspase-3 and anti-pTyr10-LDHA. **b**) LDHA activity in HEK293 cells following 2 h treatment with FLCN-10 peptide. **c**) **d**) Flow cytometric assessment of cell death in renal cell lines following 1 μM FLCN-10 for 1 or 2 h (Extended Data Fig. 9c) or 0.1 μM or 1 μM FLCN-10 treatment for 2 h (Extended Data Fig. 9d) as determined by Annexin V/Propidium iodide staining. Representative of three independent experiments. **e**) Immunoblot of whole cell lysates following overexpression of FLAG-tagged FLCN-WT, FLCN-M222A, or FLCN-F226A in normal HEK293 cells or the ccRCC cell lines 786-O, Caki-1 and Caki-2. **f**) HEK293 cells were treated with and without 1 μM Rhodamine B-labeled FLCN-10A. Scale bar = 20 μM. **g**) LDHA activity in Caki-1 cells following 2 h treatment with FLCN-10A peptide.

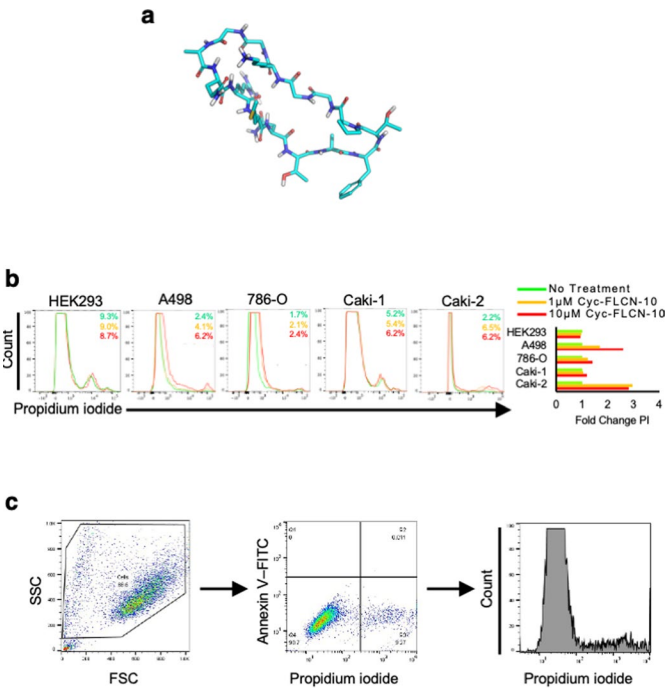

Extended Data Fig. 10 | Heterocyclic FLCN-10 peptide induces cell death in ccRCC cells. a) Structural representation of head-to-tail cyclic-FLCN-10 peptide, created using MAESTRO (Schrodinger.com). **b**) Flow cytometric assessment of cell death in renal cell lines following 1 μM or 10 μM cyclic-FLCN-10 treatment as determined by propidium iodide staining. Representative of three independent experiments. **c**) Representative flow cytometry gating strategy. Cells were first stratified by size, followed by staining intensity with Annexin V-FITC and Propidium Iodide (Extended Data Fig. 9c, d). The PI intensity signal was converted into a histogram for presentation in Fig. 5a and Extended Data Fig. 10b.

nature research

Corresponding author(s): Mehdi Mollapour & Gennady Bratslavsky

Last updated by author(s): Jun 18, 2021

Reporting Summary

Nature Research wishes to improve the reproducibility of the work that we publish. This form provides structure for consistency and transparency in reporting. For further information on Nature Research policies, see our Editorial Policies and the Editorial Policy Checklist.

Statistics

For all statistical analyses, confirm that the following items are present in the figure legend, table legend, main text, or Methods section.

n/a	Confirmed
☐	☒ The exact sample size (*n*) for each experimental group/condition, given as a discrete number and unit of measurement
☐	☒ A statement on whether measurements were taken from distinct samples or whether the same sample was measured repeatedly
☐	☒ The statistical test(s) used AND whether they are one- or two-sided *Only common tests should be described solely by name; describe more complex techniques in the Methods section.*
☒	☐ A description of all covariates tested
☒	☐ A description of any assumptions or corrections, such as tests of normality and adjustment for multiple comparisons
☐	☒ A full description of the statistical parameters including central tendency (e.g. means) or other basic estimates (e.g. regression coefficient) AND variation (e.g. standard deviation) or associated estimates of uncertainty (e.g. confidence intervals)
☐	☒ For null hypothesis testing, the test statistic (e.g. *F*, *t*, *r*) with confidence intervals, effect sizes, degrees of freedom and *P* value noted *Give P values as exact values whenever suitable.*
☒	☐ For Bayesian analysis, information on the choice of priors and Markov chain Monte Carlo settings
☒	☐ For hierarchical and complex designs, identification of the appropriate level for tests and full reporting of outcomes
☒	☐ Estimates of effect sizes (e.g. Cohen's *d*, Pearson's *r*), indicating how they were calculated

Our web collection on statistics for biologists contains articles on many of the points above.

Software and code

Policy information about availability of computer code

Data collection	Epson Perfection V700/V750, Microsoft Excel 2020/2021, FlowJo (Treestar)
Data analysis	All statistics were performed using GraphPad Prism version 7.00 for Windows (GraphPad Software, La Jolla, California, USA, https://www.graphpad.com).

For manuscripts utilizing custom algorithms or software that are central to the research but not yet described in published literature, software must be made available to editors and reviewers. We strongly encourage code deposition in a community repository (e.g. GitHub). See the Nature Research guidelines for submitting code & software for further information.

Data

Policy information about availability of data

All manuscripts must include a data availability statement. This statement should provide the following information, where applicable:

- Accession codes, unique identifiers, or web links for publicly available datasets
- A list of figures that have associated raw data
- A description of any restrictions on data availability

Data and Software Availability- All data generated or analysed during this study are included in this published article (and its supplementary information files). Proteomic data is available on the ProteomeXchange, dataset identifier PXD018410.

Field-specific reporting

Please select the one below that is the best fit for your research. If you are not sure, read the appropriate sections before making your selection.

☒ Life sciences ☐ Behavioural & social sciences ☐ Ecological, evolutionary & environmental sciences

For a reference copy of the document with all sections, see nature.com/documents/nr-reporting-summary-flat.pdf

Life sciences study design

All studies must disclose on these points even when the disclosure is negative.

Sample size	Experiments were designed to include sample sizes large enough so that the difference observed between the tested sample and the control sample is statistically significant.
Data exclusions	No data were excluded from this manuscript.
Replication	Three biological and technical replicates were used to confirm each experimental finding. All attempts were successful.
Randomization	All cell line models were split and passaged to assure homogeneity during experimentation, thus experiments were not randomized.
Blinding	No comparisons or studies requiring the use of blinding are reported in this study. Therefore no blinding of the samples was performed.

Reporting for specific materials, systems and methods

We require information from authors about some types of materials, experimental systems and methods used in many studies. Here, indicate whether each material, system or method listed is relevant to your study. If you are not sure if a list item applies to your research, read the appropriate section before selecting a response.

Materials & experimental systems

n/a	Involved in the study
☐	☒ Antibodies
☐	☒ Eukaryotic cell lines
☒	☐ Palaeontology and archaeology
☒	☐ Animals and other organisms
☐	☒ Human research participants
☒	☐ Clinical data
☒	☐ Dual use research of concern

Methods

n/a	Involved in the study
☒	☐ ChIP-seq
☐	☒ Flow cytometry
☒	☐ MRI-based neuroimaging

Antibodies

Antibodies used

Rabbit anti-FLAG tag Thermo Scientific Cat# PA1-984B; RRID:AB_347227
Mouse anti-GAPDH (1D4) Enzo Life Sciences Cat# ADI-CSA-335; RRID:AB_10617247
Rabbit anti-FLCN (D14G9) Cell Signaling Technology Cat# 3697; RRID:AB_2231646
Rabbit anti-HA tag (C29F4) Cell Signaling Technology Cat# 3724; RRID:AB_1549585
Anti-mouse secondary Cell Signaling Technology Cat# 7076; RRID:AB_330924
Anti-rabbit secondary Cell Signaling Technology Cat# 7074; RRID:AB_2099233
Anti-mouse Alexa Fluor secondary ThermoFisher Scientific Cat# A-21203; RRID:AB_2535789
Alexa Fluor® 594 Life Technologies Cat# A-21203; RRID:AB_141633
Alexa Fluor® 488 Life Technologies Cat# A-11006; RRID:AB_2534074
Anti-LDHA (E-9) Santa Cruz Biotechnology Cat# sc-137243; RRID:AB_2137192
Anti-phospho-Tyr10-LDHA Cell Signaling Technology Cat# 8176S; RRID:AB_11220238
Hoechst 33258 Millipore-Sigma Cat# 94403
Anti-Cleaved Caspase-3 (Asp175) (5A1E) Cell Signaling Technology Cat# 9664S; RRID:AB_2070042

Validation

All antibodies used in the course of this research have been validated by the manufacturer and/or previous literature. We regularly monitor the records at antibody www.registry.org to determine if other authors have raised issues with any of the antibodies listed. Validation was based on the manufacturer's recommendation website, These include https://www.cellsignal.com/; https://www.enzolifesciences.com/; https://www.thermofisher.com/; https://www.emdmillipore.com/US/en

Eukaryotic cell lines

Policy information about cell lines

Cell line source(s)	HEK293 (Female) ATCC Cat# CRL-1573; RRID:CVCL_0045 HAP1 WT (Male) Horizon Discovery RRID:CVCL_TY20 HAP1 LDHA KO (Male) Horizon Discovery Cat# HZGHC004917c002; RRID:CVCL_SV40 HAP1 LDHB KO (Male) Horizon Discovery Cat# HZGHC005907c010; RRID:CVCL_SV42 UOK257 (Male) LSS RRID:CVCL_S717 UOK257-2 (Male) LSS RRID:CVCL_1D69 Du145 (Male) ATCC Cat# HTP-81; RRID:CVCL_0105 J82 (Male) ATCC Cat# HTB-1; RRID:CVCL_0359 UM-UC-3 (Male) ATCC Cat# CRL-1749; RRID:CVCL_1783 MDA-MB-231 (Female) ATCC Cat# HTB-26; RRID:CVCL_0062 A549 (Male) ATCC Cat# CRM-CCL-185; RRID:CVCL_0023 786-O (Male) ATCC Cat# CRL-1932; RRID:CVCL_1051 PC3 (Male) ATCC Cat# CRL-1435; RRID:CVCL_0035 SW780 (Female) ATCC Cat# CRL-2169; RRID:CVCL_1728 LNCaP (Male) ATCC Cat# CRL-1740; RRID:CVCL_1379 H1299 (Male) ATCC Cat# CRL-5803; RRID:CVCL_0060 A498 (Female) ATCC Cat# CRL-44; RRID:CVCL_1056 Caki-1 (Male) ATCC Cat# HTB-46; RRID:CVCL_0234 Caki-2 (Male) ATCC Cat# HTB-47; RRID:CVCL_0235 HT29 (Female) ATCC Cat# HTB-38; RRID:CVCL_0320 T24 (Female) ATCC Cat# HTB-4; RRID:CVCL_0554 RT4 (Male) ATCC Cat# CRL-7937; RRID:CVCL_0036
Authentication	To verify that these are not false cell lines, misidentified, and are authentic stock we will periodically check the Cellosaurus web pages as we understand that this resource houses the most up to date information on cell line misidentification and works closely with cell line repositories. Authentication testing has been performed on established cell lines regardless of the application. Testing will be done, at minimum, at the beginning and end of experimental work. For human cell lines, short tandem repeat (STR) profiling will be performed and compared to results from donor tissue, or to online databases of human cell line STR profiles (ANSI/ATCC ASN-0002-2011 Authentication of Human Cell Lines: Standardization of STR Profiling. ANSI eStandard Store.)
Mycoplasma contamination	All cell lines have tested negative for mycoplasma contamination.
Commonly misidentified lines (See ICLAC register)	none

Human research participants

Policy information about studies involving human research participants

Population characteristics	Characteristics of the human research participant relates to their rare type of cancer,
Recruitment	Only one patient was recruited through Urology clinic at Upstate medical university to this study, as this study concerns a rare genetic subtype of kidney cancer present in only ~2,000 patients worldwide.
Ethics oversight	SUNY Upstate Medical University Institutional Review Board

Note that full information on the approval of the study protocol must also be provided in the manuscript.

Flow Cytometry

Plots

Confirm that:

☒ The axis labels state the marker and fluorochrome used (e.g. CD4-FITC).

☒ The axis scales are clearly visible. Include numbers along axes only for bottom left plot of group (a 'group' is an analysis of identical markers).

☒ All plots are contour plots with outliers or pseudocolor plots.

☒ A numerical value for number of cells or percentage (with statistics) is provided.

Methodology

Sample preparation	Cells were trypsinized, collected, and washed once with 1x binding buffer (included in Annexin V:FITC kit (Bio-Rad)). Annexin V-FITC was added at 1:40 and incubated for 10 min at room temperature in the dark. Following one wash with 1x binding buffer, propidium iodide was added.

Instrument	Becton Dickinson LSRFortessa (BD Biosciences)
Software	FlowJo software v10.6.2 (BD).
Cell population abundance	Fewer than 25% of cells were found to be positive for Annexin V/PI in any given sample.
Gating strategy	"Live" cells (any calls between the axes of the FSC/SSC plot) were gated and Annexin V/PI positivity was determined using a quadrant gate. Dot plots of Annexin V/PI can be found in the supplementary information.

☒ Tick this box to confirm that a figure exemplifying the gating strategy is provided in the Supplementary Information.